

Three-dimensional force microscopy of cells in biopolymer networks

Julian Steinwachs¹, Claus Metzner¹, Kai Skodzek¹, Nadine Lang¹, Ingo Thievesen¹, Christoph Mark¹, Stefan Münster², Katerina E Aifantis³ & Ben Fabry¹

We describe a technique for the quantitative measurement of cell-generated forces in highly nonlinear three-dimensional biopolymer networks that mimic the physiological situation of living cells. We computed forces of MDA-MB-231 breast carcinoma cells from the measured network deformations around the cells using a finite-element approach based on a constitutive equation that captures the complex mechanical properties of diverse biopolymers such as collagen gels, fibrin gels and Matrigel. Our measurements show that breast carcinoma cells cultured in collagen gels generated nearly constant forces regardless of the collagen concentration and matrix stiffness. Furthermore, time-lapse force measurements showed that these cells migrated in a gliding motion with alternating phases of high and low contractility, elongation, migratory speed and persistence.

The migration of cells through the fibrous network of the extracellular matrix is an integral part of many biological processes, including tissue morphogenesis, wound healing and cancer metastasis¹. To migrate through the pores of the dense meshwork of the extracellular matrix, cells must generate considerable forces that are exerted on the matrix^{2–5}. Accurate measurement of these traction forces is crucial for understanding the invasion of cancer cells or the migration of immune cells in tissue^{5,6}.

One can estimate traction forces by culturing cells on artificial two-dimensional (2D) or three-dimensional (3D) substrates with known stiffness and measuring the substrate deformations as the cells adhere and migrate^{7–11}. Present methods for traction-force reconstruction rely on the linear force-displacement response of the substrate. However, the connective tissues of most organs are highly nonlinear, as are reconstituted tissue equivalents such as collagen and fibrin gels, both of which stiffen strongly under shear^{12–14} and collapse with an abnormal apparent Poisson's ratio greater than 1 when stretched^{15–18} (Fig. 1).

In this report we describe a method for measuring cell traction forces in physiologically relevant 3D biopolymer networks with highly nonlinear mechanical properties. With our method, we studied the contractility, migration and shape changes of breast

carcinoma cells in collagen gels with differing concentrations and matrix stiffness. During migration, breast carcinoma cells underwent alternating phases of high and low contractility, elongation, migratory speed and persistence, all of which showed high temporal correlation. On average, these cells did not respond to higher matrix stiffness with greater contractility, which can be partially explained by impaired cell elongation in denser gels.

RESULTS

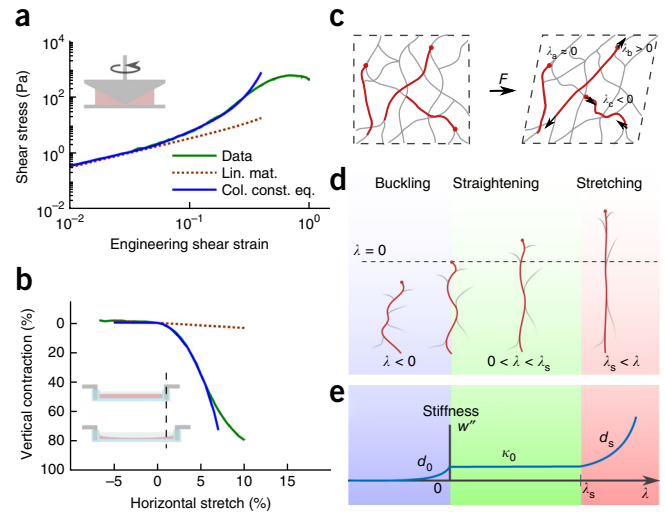
Macrorheology and constitutive equation for collagen gels

To measure 3D cell traction from the deformation of the surrounding collagen network matrix, we combined existing micromechanical models with a continuum description: on a small spatial scale corresponding to a fiber segment, we considered that the local deformation of the fiber segment does not follow the deformation of the bulk. This so-called non-affine behavior is caused by fiber buckling, straightening or stretching^{14,19–24} and gives rise to a pronounced nonlinear stress-strain relationship and collapse of the material under uniaxial stretch (Fig. 1a,b). Beyond the length scale of the typical interconnection distance, however, the strain of the fiber approximates the macroscopic strain λ (ref. 14), depending on the orientation of the fiber and the applied deformation (equation (2)). We assumed that deformations become affine for a sufficiently large volume of material, and thus we were able to compute the stress-strain response by averaging the force contributions of all fibers contained in such a volume¹² (Fig. 1c).

The mechanical properties of collagen fibers can be described by a nonlinear potential function $w(\lambda)$ with stiffness $w''(\lambda)$ that exhibits three distinct regimes (equation (1)). Under compression, the fibers buckle, and the stiffness falls exponentially with a characteristic strain scale d_0 . For small extensions, the fibers have a constant stiffness κ_0 . If the fibers are stretched beyond the linear strain range λ_s , the stiffness increases exponentially with a characteristic strain scale d_s (Fig. 1e). By averaging the stress contributions of many fibers¹², assuming an isotropic and homogeneous distribution (Supplementary Notes 1–3), one can derive a constitutive equation (equation (3)) that describes the mechanical behavior of the bulk material.

¹Department of Physics, University of Erlangen-Nuremberg, Erlangen, Germany. ²Department of Biological Physics, Max Planck Institute for the Physics of Complex Systems, Dresden, Germany. ³Department of Civil Engineering and Engineering Mechanics, University of Arizona, Tucson, Arizona, USA. Correspondence should be addressed to J.S. (julian.steinwachs@fau.de).

Figure 1 | Macrorheology of collagen type I gels and semi-affine model description. **(a)** Shear stress versus shear strain of a 2.4-mg ml⁻¹ collagen gel measured in a cone-plate rheometer (representative of $n = 5$). Lin. mat., predictions from a linear material model; Col. const. eq., predictions from a constitutive equation for collagen gels. **(b)** Vertical contraction and expansion of a 2.4-mg ml⁻¹ collagen gel under uniaxial compression and stretch. Lines color-coded according to the key in **a**. **(c)** Non-affine deformations (stretch and compression) of individual collagen fibers, depending on their orientation. **(d)** Fiber buckling under compressional strain ($\lambda < 0$), fiber straightening under small extensional strain ($0 < \lambda < \lambda_s$) and fiber stretching under large extensional strain ($\lambda_s < \lambda$). **(e)** Fiber stiffness versus fiber strain ($w''(\lambda)$) for the same regimes shown in **d**, characterized by an exponential decrease with a characteristic strain scale d_0 for buckling, a constant stiffness κ_0 for small extensional strain and an exponential increase with a characteristic strain scale d_s for large extensional strain.



We determined the four parameters of our constitutive equation (d_0 , κ_0 , λ_s and d_s) by means of two types of experiments. First, we measured the stress-strain relationship for simple shear deformation in a cone-plate rheometer (**Fig. 1a**). We found a linear regime followed by pronounced strain stiffening beyond a shear of $\sim 3\%$ that was well described by an exponential behavior^{13,16,21}. Second, we measured the vertical (z) contraction of collagen gel when it was uniaxially stretched in the x -direction while the strain in the y -direction was fixed at 0% (**Fig. 1b**). Collagen gels exhibited strong vertical contraction under stretch, with a horizontal-to-vertical stretch ratio of ~ 8 (**Fig. 1b**), indicating an apparent Poisson's ratio considerably greater than 1. Additionally, we measured the horizontal gel dilation under uniaxial compression. The gel expanded only weakly in the vertical direction, revealing the fundamental asymmetry of the material resulting from fiber buckling (**Fig. 1b**).

Our material model (equation (3)) reproduced our experimental data (the strain stiffening, the high apparent Poisson's ratio and the stretch-versus-compression asymmetry) well up to 30% of compression, 30% of shear and 7% of uniaxial stretch (**Fig. 1**). Moreover, measurements of collagen gels with different concentrations (0.6, 1.2 and 2.4 mg ml⁻¹), fibrin gels and Matrigel showed that our material model captured the rheology of these biopolymer networks (**Supplementary Notes 4–8**).

This constitutive equation allowed us to compute the gel deformations and stress in response to arbitrary forces, geometries and boundary conditions using a finite-element approach. For finite-element analysis, we represented the geometry of the gel with a mechanically coupled mesh of simple tetrahedra (**Supplementary Note 2**). Our analysis showed that collagen gels stiffened strongly under dilating forces of cells, resulting in steric hindrance against migration (**Supplementary Note 9**). In contrast, gel stiffening was weak with contracting cell forces. This mechanical behavior of collagen gels led to more efficient migration for elongated cells with polarized tractions (**Supplementary Note 9**).

Experimental validation with point-like forces

To experimentally test the validity of the material model in combination with the finite-element approach, we applied forces of 10–30 nN using 5- μ m magnetic beads attached to the surface of a collagen gel in a magnetic-tweezers setup (**Fig. 2a,b**). We measured the resulting local gel displacement by tracking fluorescent marker beads in the gel (**Fig. 2c**). Time-lapse recordings

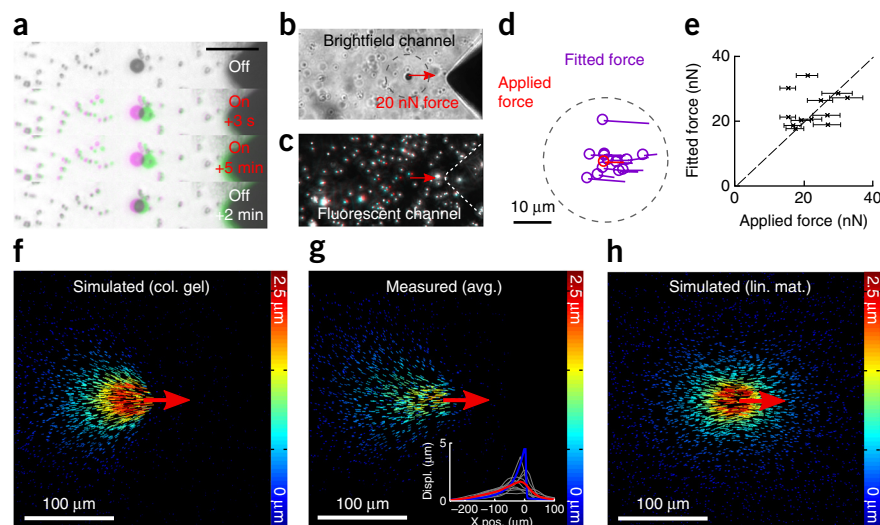
of the matrix response showed predominantly elastic behavior with negligible viscosity and plasticity (**Fig. 2** and **Supplementary Note 10**). We then predicted the local gel displacement from the known magnetic forces and the mechanical parameters of the gel as measured with an extensional rheometer (**Fig. 2f–h** and **Supplementary Note 5**). The predicted displacement field overestimated the maximum displacement near the bead but was in good agreement with measurements at distances of more than 50 μ m from the point of force application (**Fig. 2g**). In particular, our measurements confirmed the model prediction of a highly asymmetric displacement field. We found that the gel deformed strongly under tension (**Fig. 2**) but not under compression, as compressive stresses propagated poorly owing to fiber buckling. By contrast, the displacement field in a linear material (**Fig. 2h**) was centered on the external force.

In a second test, we reconstructed the applied point-like force of the magnetic bead from the measured collagen displacement field. We minimized the mismatch between the simulated and the measured local gel displacement by adjusting the position, direction and magnitude of the simulated force. The fitted force position, on average, coincided precisely with the centroid of the measured bead position, with an s.d. of 4 μ m for different measurements (**Fig. 2d**). The fitted force amplitude was on average 22% higher than the applied magnetic force, with an s.d. of 33% for different measurements (**Fig. 2e**).

Unconstrained 3D force reconstruction

In contrast to the point-like force on a magnetic bead, the spatial distribution of forces around living cells is unknown. Unconstrained force reconstruction does not rely on cell-surface information and makes no prior assumptions about the 3D force field of the cell. This creates a computational problem, as the number of fit parameters (force vectors) is the same as the number of measured data points (displacement vectors). To prevent overfitting, we introduced a regularization approach that allowed cell forces to be present only in a portion of the measured volume. Each node of the finite-element mesh was assigned a weight with which external forces at that node were penalized. When the penalty was iteratively lowered for nodes with high forces, the prevailing cell forces condensed onto a few nodes, and small forces due to uncorrelated measurement noise were minimized

Figure 2 | Experimental validation of the constitutive equation for collagen gels. (a) Image recordings (representative of 13 measurements) of the magnetic bead, small fiducial marker beads and the magnetic needle tip during force application at different time points (in green) overlaid with an image of the unstrained configuration (in magenta). Colors from fiducial markers that did not move grade to black. Scale bar, 20 μm . (b) Brightfield image of the magnetic-tweezers experiment. The dashed circle corresponds to the dashed circle in d. (c) Overlay of fluorescent images of the marker beads before (cyan) and after (red) a force of 20 nN was applied to the beads. Red arrow indicates the direction of the applied force as in b. (d) Reconstructed forces (position, direction and magnitude) of magnetic beads from 13 independent measurements. The length of the lines is normalized to the magnitude of the known applied force (red). The dashed circle corresponds to the dashed circle in b. (e) Reconstructed force magnitude versus applied force magnitude. Horizontal error bars indicate the error (r.m.s.) in the applied force due to variations in bead size. (f) Simulated displacement around a point-like force of 20 nN. Col. gel., collagen gel. (g) Measured displacement around a point-like force of 20 nN averaged (avg.) over 13 measurements. Inset shows the local matrix displacements (Displ.) along the x -axis through the point of force application (at $x = 0$). Simulated displacements are shown in blue, individual measurements from different beads are in gray, and the average is in red. Pos., position. (h) Simulated displacements around a point-like force of 20 nN for a linear material (lin. mat.).



in the rest of the volume. The strength of the regularization was controlled by the parameter α . By running unconstrained force reconstruction on the above-described data set of matrix displacements around a point-like force, we found that the total force (the vector sum of all forces around the magnetic bead) depended little on α for values less than $0.3 \text{ pN}^2 \mu\text{m}^{-2}$ (Supplementary Note 11). The systematic force error was less than 1% with an s.d. of 30% between individual measurements. When averaged over many beads, however, the reconstructed forces appeared blurred and were systematically shifted 30 μm away from the direction of force application (Discussion).

Traction forces of living cells

To measure the force-induced deformation of a collagen gel, we imaged the collagen network around the cells with confocal

reflection microscopy before and after force relaxation with cytochalasin D and evaluated the local displacement field via 3D particle image velocimetry (Fig. 3 and Supplementary Note 12). Unconstrained reconstructed cellular forces were localized near but not exactly on the surfaces of cells (Fig. 3b,c). To quantify this error, we projected the cellular force together with brightfield images of a given cell onto the x - y plane and plotted the average force density versus the distance to the cell edge. Forces were systematically shifted away from the cell edge by approximately 18 μm (Fig. 3f) (see Discussion).

In addition to cell forces, our model allowed us to compute the principal matrix stress (Fig. 3d) and the principal matrix stiffness (Fig. 3e). Both tended toward zero in the region of the cell where the material was compressed and the fibers buckled, in essence creating a hole where the contracting cell was located. This suggests that cell forces are used almost exclusively to pull collagen fibers centripetally toward the cell. Therefore, our approach describing cellular forces as a 3D force field in a

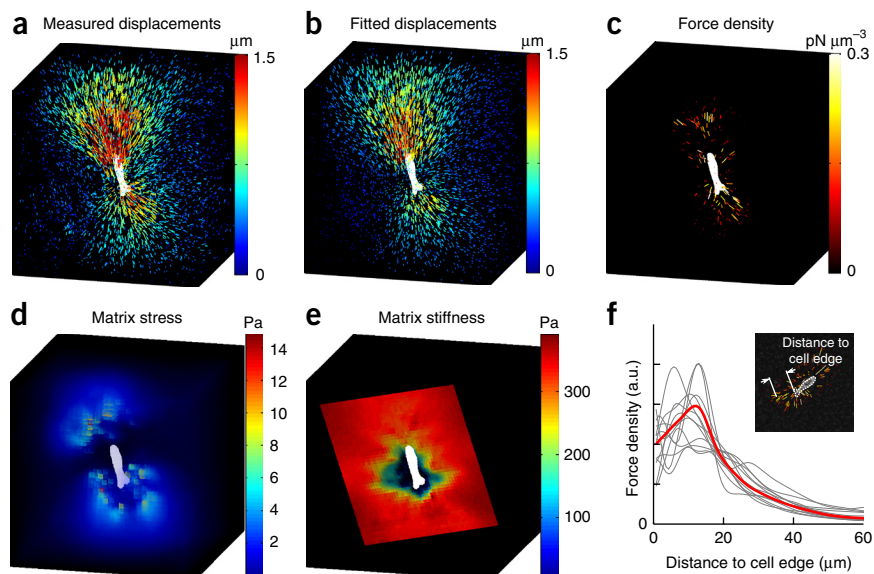


Figure 3 | Reconstruction of cellular forces inside a 1.2-mg ml^{-1} collagen gel. (a) Measured displacements around a single MDA-MB-231 breast carcinoma cell. (b) Regularized displacement field around the cell in a. (c) Force density around the cell in a and b as calculated from the regularized displacements shown in b. (d) Principal matrix stress as calculated from the regularized displacement field. (e) Principal matrix stiffness as calculated from the regularized displacement field. (f) Reconstructed force density in arbitrary units (a.u.) around individual cells ($n = 12$; gray curves) as a function of the distance to the cell edge as illustrated in the inset. The average force density is shown in red.

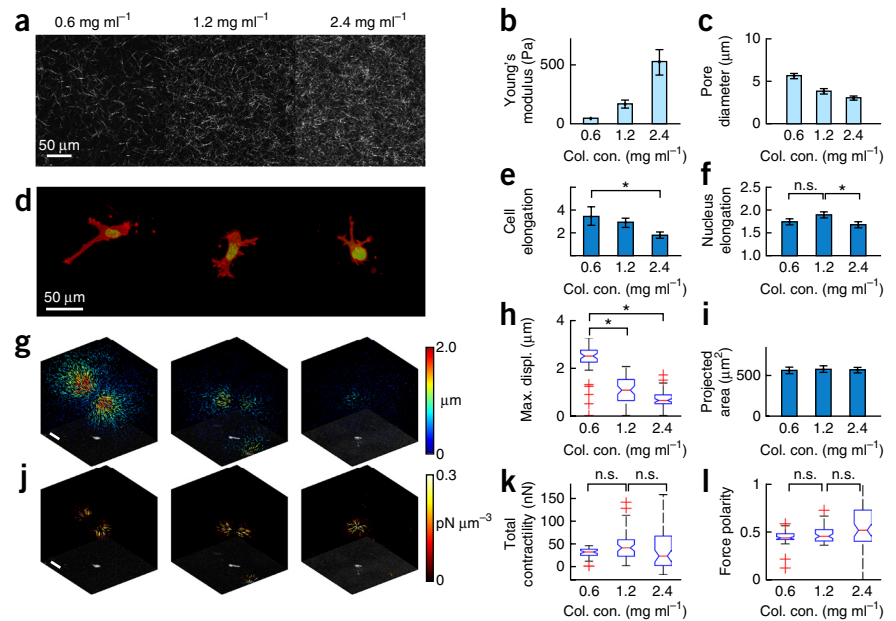
Figure 4 | Contractility of MDA-MB-231 cells in gels with different collagen concentrations.

(a) Collagen fiber network imaged using confocal reflection microscopy. (b,c) Linear Young's modulus of collagen gels (b) and pore diameter of the network (c).

(d) Morphology of cells (actin in red, chromatin in green) embedded in collagen gel. (e,f) Cell elongation (e) and elongation of the nucleus (f) in cells embedded in collagen gel. (g) 3D matrix displacement fields of the collagen gel around embedded cells. Density and hue of marks indicate the magnitude of the local displacement vector. (h) Maximum cell-induced matrix displacement (Max. displ.). (i) Projected area of cells embedded in collagen gel. (j) 3D force density of cells embedded in collagen gels. Density and color intensity of marks are proportional to the local force density. Scale bars in g,j, 50 μm . (k,l) Total contractility (k) and force polarity (l) of cells in collagen gel.

For all box plots, the central (red) mark indicates the median, the edges of the box denote the 25th and 75th percentiles, the whiskers extend to the most extreme data points not considered outliers, and outliers are plotted individually (red crosses).

* $P \leq 0.05$, Student's t -test assuming unequal variances including the outliers. Col. con., collagen concentration; n.s., not significant ($P > 0.05$).



continuous material, without a 'hole' to accommodate the cell, does not lead to force overestimation¹¹.

As a measure of cell contractility, we quantified the total magnitude of the projected force vectors pointing toward the cell center (Supplementary Note 13). From a data set of 63 MDA-MB-231 cells in a 1.2-mg ml⁻¹ collagen gel, we measured a total contractility of 47.6 ± 3.4 nN (geometric mean \pm s.e.m.). The total contractility for the same cell line grown on a planar collagen-coated polyacrylamide substrate (Young's modulus: 5 kPa) has been reported^{25,26} as ~ 270 nN.

To quantify the geometry of the 3D cellular force fields, we decomposed the contractile force into force contributions from three principal components of an orthogonal coordinate system aligned with the force field of the cell (Supplementary Note 13). For a force dipole, the force polarity approaches 1, whereas for an isotropic force field, the force polarity approaches 1/3. The force polarity of MDA-MB-231 cells was 0.47 ± 0.01 (mean \pm s.e.m., $n = 63$), indicating that about half of the total contractility could be expressed by a single force dipole.

Contractile cell forces contribute to the strain stiffening of a collagen matrix surrounding cells. To quantify this, we computed for every cell the mechanical work needed to achieve a small additional matrix deformation. MDA-MB-231 cells stiffened the bulk of the collagen gel on average by $3.2\% \pm 0.5\%$ (mean \pm s.e.m.), in agreement with numerical simulations that also indicated little strain stiffening of the bulk of the collagen matrix around contractile cells (Supplementary Note 9). In contrast, the collagen matrix showed a pronounced stiffening response to dilatational forces that occur when a cell is attempting to squeeze through a narrow pore (Supplementary Note 9).

Constrained 3D force reconstruction

Unconstrained force reconstruction can robustly resolve total cell contractility down to 5 nN for displacement noise levels in excess of 200 nm, but the method has limited localization accuracy (Fig. 3f

and Supplementary Notes 14–17). To avoid the systematic shift and blurring of the reconstructed forces, one can constrain their localization to the cell surface. To demonstrate this, we fluorescently stained the cytoplasm of HT1080 fibrosarcoma cells, imaged the cells with confocal microscopy, and segmented them by thresholding. We assigned a zero-penalty weight to nodes of finite elements with a distance to the cell surface of less than half the mesh size; the remaining computation was identical to the unconstrained method. The force localization of the constrained method was superior to that of the unconstrained method (Supplementary Note 18), but both methods gave similar values for the total contractility and force polarity.

Traction forces in gels of varying collagen concentration

To study how cells respond to changes in matrix stiffness and density, we measured traction forces of MDA-MB-231 cells embedded in collagen gels with different concentrations (0.6 ($n = 48$), 1.2 ($n = 63$) and 2.4 mg ml⁻¹ ($n = 64$)) where the linear stiffness increased from 44 Pa to 513 Pa and the average pore diameter decreased from 5.6 μm to 3.0 μm (Fig. 4a–c)²⁷. Fluorescent staining of the actin cytoskeleton showed that cells in the denser gels were more rounded and had smaller and thinner protrusions than cells in gels with lower collagen concentrations (Fig. 4d–f). However, the projected cell area in these different gels, and therefore the cell volume, was the same. Matrix deformations induced by the cells decreased with increasing collagen concentration (Fig. 4g–i), but the total cell contractility, measured using unconstrained force reconstruction, remained the same, as did the force polarity (Fig. 4j–l and Supplementary Note 19).

Time-lapse force microscopy

Reflection microscopy minimizes photodamage and allows for long-term measurements (>24 h) of migration trajectories, cell morphology and traction forces (Supplementary Videos 1 and 2). To investigate the coordination of traction forces during cell migration

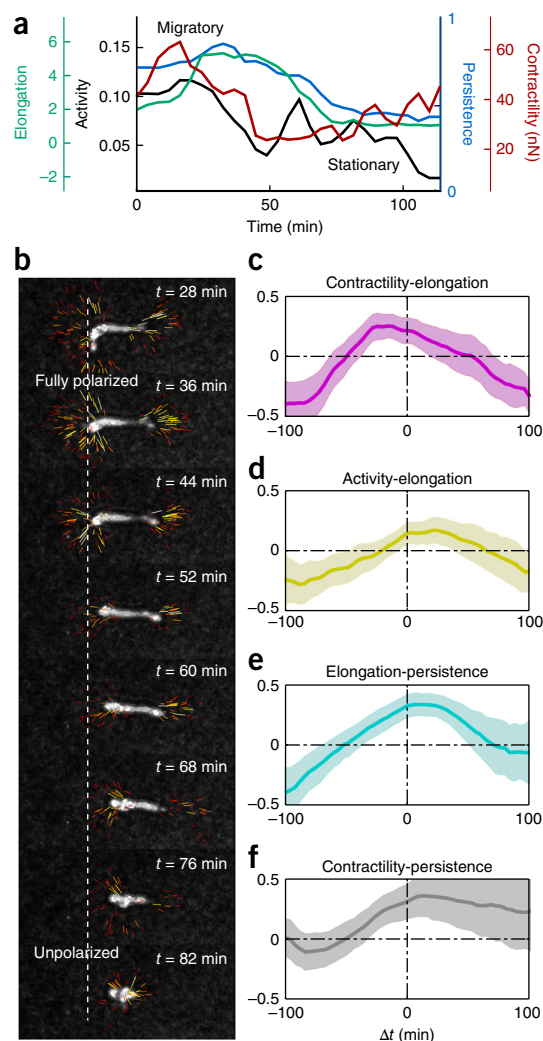


Figure 5 | Time-lapse force microscopy of a breast carcinoma cell inside collagen gel. **(a)** Time course of contractility, elongation, migratory activity and migratory persistence of an MDA-MB-231 breast carcinoma cell embedded in a 3D collagen gel (1.2 mg ml^{-1}). **(b)** Force field of the cell shown in **a**. **(c–f)** Cross-correlation of force fluctuations, cell morphology and migration parameters for different time lags averaged over 20 cells. **(c)** Contractility versus elongation. **(d)** Activity versus elongation. **(e)** Elongation versus persistence. **(f)** Contractility versus persistence. Shaded area around curves indicates ± 1 s.e.

through a disordered 3D collagen matrix, we simultaneously measured the time course of contractility, cell elongation, migration persistence p and migration activity a (calculated from the momentary cell speed v according to $a = v(1 - p^2)^{0.5}$ (Fig. 5a,b)²⁸). We found that for MDA-MB-231 cells, all four parameters were significantly correlated for time lags between 0 and ± 15 min (Fig. 5c–f and Supplementary Note 20). This implies that phases of rapid cell movements with high persistence and activity were accompanied by large contractile forces and pronounced cell elongation. Conversely, phases during which the cells remained stationary were accompanied by small contractile forces and more rounded cell shapes. For lag times greater than ± 1 h, the correlations between these parameters were negative, implying that migratory phases lasted for approximately 1 h. Moreover, phases of high contractility were accompanied by further cell lengthening (Supplementary Note 20).

DISCUSSION

Our underlying assumption of the biopolymer network as a mechanical continuum is violated at the scale of individual fibers or single network pores. Therefore, the spatial resolution of the reconstructed forces is limited by the length scale at which the continuum assumption breaks down. Accordingly, we attribute the variability and positional errors in reconstructed forces in the magnetic bead experiments (Fig. 2g) to local heterogeneity in the fiber structure of the gels (density, fiber orientation, fiber thickness and connectivity) as described previously²⁹. The spatial resolution of the reconstructed force is therefore limited to around $30 \mu\text{m}$ (Supplementary Note 11). Further, blurring of the reconstructed forces is caused by the size of the finite elements, the presence of measurement noise and the necessary regularization (Supplementary Note 14). Finally, collagen fibers under compression can bear only little mechanical stress, and therefore all discrepancies between the continuum model and the real situation of an inhomogeneous collagen gel must be reconciled by forces that arise in the tensed region of the collagen gel. If confocal image stacks of fluorescently labeled cells are available, one can avoid this problem by restricting the reconstructed forces to the cell surface (Supplementary Note 18).

Our statistical force fluctuations of 30% due to measurement errors are considerably smaller than the $>50\%$ fluctuations in the total force magnitude between individual cells (Fig. 4k). Therefore, our measurement error does not markedly degrade the quality of the data or require the measurement of a considerably larger number of cells for statistical significance. Table 1 summarizes the sensitivity, accuracy and spatial resolution of the constrained and unconstrained 3D force reconstruction methods.

Our finding of constant traction forces for collagen gels of different densities and stiffness is in contrast to cell behavior on planar substrates, where cell tractions increase with higher substrate stiffness and with increasing ligand density^{30–32}. A possible explanation that reconciles these conflicting findings is that a smaller pore size in the denser and stiffer 3D matrices may impede cell elongation and the formation of cell protrusions, and hence may reduce force generation. In support of this hypothesis, we found that the contractility of a subpopulation of elongated cells with an aspect ratio greater than 2.0 was significantly ($P < 0.05$, Student's two-tailed t -test assuming unequal variances) greater in 1.2 mg ml^{-1} collagen gels than in 0.6 mg ml^{-1} collagen gels (Supplementary Note 21).

Our method can be used to study the dynamics of cell migration in a 3D environment. We noted that untreated MDA-MB-231 cells alternated between highly migratory and more stationary phases. During migratory phases cells had an elongated shape and high contractility. The cross-correlation between these parameters was highest for a time lag of zero. Thus we found no evidence that phases of elongation, contraction and motility

Table 1 | Sensitivity, accuracy (error) and spatial resolution of 3D force reconstruction

	Unconstrained	Constrained
Sensitivity	5 nN ^a	5 nN ^a
Error (relative bias \pm s.d.)	$<1\% \pm 30\%$ ^b	$+22\% \pm 33\%$ ^b
Spatial resolution (bias \pm s.d.)	$30 \mu\text{m} \pm 30 \mu\text{m}$ ^{b,c}	$0 \mu\text{m} \pm 4 \mu\text{m}$ ^b

^aFor a 384-Pa (Young's modulus) collagen gel and 60-nm spatial resolution of local gel displacement. ^bFor a point force of 10–30 nN. ^cSpatial bias is in the force direction.

are shifted relative to one another, as one would expect with an ‘inchworm’ type of motion in which contraction leads to cell shortening and force relaxation leads to cell lengthening. Rather, during the migratory phases, MDA-MB-231 cells seemed to glide through the gel in a steady process of simultaneous adhesion and de-adhesion.

These results demonstrate that our 3D traction force microscopy method can contribute to understanding of the physical mechanisms of cell migration in physiologically relevant environments.

METHODS

Methods and any associated references are available in the [online version of the paper](#).

Note: Any Supplementary Information and Source Data files are available in the online version of the paper.

ACKNOWLEDGMENTS

We thank J.P. Butler (Harvard University) for helpful discussions and for developing a method to locate the force epicenter from a 3D vector field, and we thank P. Strissel (University Clinics Erlangen) for help with Matrigel experiments. We acknowledge E. Wagena (Radboud University Nijmegen) for generating dual-color HT1080 fibrosarcoma cells, which were a gift from K. Wolf (Radboud University Nijmegen, the Netherlands). This work was supported by the German Research Foundation (DFG) Research Training Group 1962 “Dynamic Interactions at Biological Membranes: From Single Molecules to Tissue,” the US National Institutes of Health (NIH-HL65960) and the Emerging Fields Initiative of the University of Erlangen–Nuremberg.

AUTHOR CONTRIBUTIONS

J.S., B.F., S.M., I.T., N.L. and K.S. designed the setup and performed the experiments; J.S., C. Metzner and K.E.A. developed the material model and mathematical tools; J.S., C. Metzner and C. Mark wrote the data-acquisition and analysis software; J.S., S.M. and B.F. wrote the article.

COMPETING FINANCIAL INTERESTS

The authors declare no competing financial interests.

Reprints and permissions information is available online at <http://www.nature.com/reprints/index.html>.

- Friedl, P., Zanker, K.S. & Brocker, E.B. Cell migration strategies in 3-D extracellular matrix: differences in morphology, cell matrix interactions, and integrin function. *Microsc. Res. Tech.* **43**, 369–378 (1998).
- Zaman, M.H. *et al.* Migration of tumor cells in 3D matrices is governed by matrix stiffness along with cell-matrix adhesion and proteolysis. *Proc. Natl. Acad. Sci. USA* **103**, 10889–10894 (2006).
- Friedl, P. & Wolf, K. Proteolytic interstitial cell migration: a five-step process. *Cancer Metastasis Rev.* **28**, 129–135 (2009).
- Friedl, P., Wolf, K. & Lammerding, J. Nuclear mechanics during cell migration. *Curr. Opin. Cell Biol.* **23**, 55–64 (2011).
- Koch, T.M., Muenster, S., Bonakdar, N., Buttler, J.P. & Fabry, B. 3D traction forces in cancer cell invasion. *PLoS ONE* **7**, e33476 (2012).
- Lämmermann, T. *et al.* Rapid leukocyte migration by integrin-independent flowing and squeezing. *Nature* **453**, 51–55 (2008).
- Dembo, M. & Wang, Y.L. Stresses at the cell-to-substrate interface during locomotion of fibroblasts. *Biophys. J.* **76**, 2307–2316 (1999).
- Butler, J.P., Tolic-Norrelykke, I.M., Fabry, B. & Fredberg, J.J. Traction fields, moments, and strain energy that cells exert on their surroundings. *Am. J. Physiol. Cell Physiol.* **282**, C595–C605 (2002).
- Sabass, B., Gardel, M.L., Waterman, C.M. & Schwarz, U.S. High resolution traction force microscopy based on experimental and computational advances. *Biophys. J.* **94**, 207–220 (2008).
- Legant, W.R. *et al.* Multidimensional traction force microscopy reveals out-of-plane rotational moments about focal adhesions. *Proc. Natl. Acad. Sci. USA* **110**, 881–886 (2013).
- Legant, W.R. *et al.* Measurement of mechanical tractions exerted by cells in three-dimensional matrices. *Nat. Methods* **7**, 969–971 (2010).
- Storm, C., Pastore, J.J., MacKintosh, F.C., Lubensky, T.C. & Janmey, P.A. Nonlinear elasticity in biological gels. *Nature* **435**, 191–194 (2005).
- Arevalo, R.C., Urbach, J.S. & Blair, D.L. Size-dependent rheology of type-I collagen networks. *Biophys. J.* **99**, L65–L67 (2010).
- Münster, S. *et al.* Strain history dependence of the nonlinear stress response of fibrin and collagen networks. *Proc. Natl. Acad. Sci. USA* **110**, 12197–12202 (2013).
- Voytik-Harbin, S.L., Roeder, B.A., Sturgis, J.E., Kokini, K. & Robinson, J.P. Simultaneous mechanical loading and confocal reflection microscopy for three-dimensional biomechanical analysis of biomaterials and tissue constructs. *Microsc. Microanal.* **9**, 74–85 (2003).
- Vader, D., Kabla, A., Weitz, D. & Mahadevan, L. Strain-induced alignment in collagen gels. *PLoS ONE* **4**, e5902 (2009).
- Roeder, B.A., Kokini, K. & Voytik-Harbin, S.L. Fibril microstructure affects strain transmission within collagen extracellular matrices. *J. Biomech. Eng.* **131**, 031004 (2009).
- Brown, A.E., Litvinov, R.I., Discher, D.E., Purohit, P.K. & Weisel, J.W. Multiscale mechanics of fibrin polymer: gel stretching with protein unfolding and loss of water. *Science* **325**, 741–744 (2009).
- Onck, P.R., Koeman, T., van Dillen, T. & van der Giessen, E. Alternative explanation of stiffening in cross-linked semiflexible networks. *Phys. Rev. Lett.* **95**, 178102 (2005).
- Heussinger, C., Schaefer, B. & Frey, E. Nonaffine rubber elasticity for stiff polymer networks. *Phys. Rev. E* **76**, 031906 (2007).
- Stein, A.M., Vader, D.A., Weitz, D.A. & Sander, L.M. The micromechanics of three-dimensional collagen-I gels. *Complexity* **16**, 22–28 (2011).
- Sheinman, M., Broedersz, C.P. & MacKintosh, F.C. Nonlinear effective-medium theory of disordered spring networks. *Phys. Rev. E* **85**, 021801 (2012).
- Stylianopoulos, T. & Barocas, V.H. Volume-averaging theory for the study of the mechanics of collagen networks. *Comput. Methods Appl. Mech. Eng.* **196**, 2981–2990 (2007).
- Licup, A.J. *et al.* Stress controls the mechanics of collagen networks. *Proc. Natl. Acad. Sci. USA* **112**, 9573–9578 (2015).
- Kranning-Rush, C.M., Carey, S.P., Califano, J.P., Smith, B.N. & Reinhart-King, C.A. The role of the cytoskeleton in cellular force generation in 2D and 3D environments. *Phys. Biol.* **8**, 015009 (2011).
- Lautscham, L.A. *et al.* Migration in confined 3D environments is determined by a combination of adhesiveness, nuclear volume, contractility, and cell stiffness. *Biophys. J.* **109**, 900–913 (2015).
- Lang, N.R. *et al.* Estimating the 3D pore size distribution of biopolymer networks from directionally biased data. *Biophys. J.* **105**, 1967–1975 (2013).
- Metzner, C. *et al.* Superstatistical analysis and modelling of heterogeneous random walks. *Nat. Commun.* **6**, 7516 (2015).
- Mickel, W. *et al.* Robust pore size analysis of filamentous networks from 3D confocal microscopy. *Biophys. J.* **95**, 6072–6080 (2008).
- Pelham, R.J. Jr. & Wang, Y. Cell locomotion and focal adhesions are regulated by substrate flexibility. *Proc. Natl. Acad. Sci. USA* **94**, 13661–13665 (1997).
- Engler, A. *et al.* Substrate compliance versus ligand density in cell on gel responses. *Biophys. J.* **86**, 617–628 (2004).
- Reinhart-King, C.A., Dembo, M. & Hammer, D.A. The dynamics and mechanics of endothelial cell spreading. *Biophys. J.* **89**, 676–689 (2005).

ONLINE METHODS

Biopolymer gel synthesis. We mixed rat tail collagen (Collagen R, 2 mg/ml, Matrix Bioscience, Berlin, Germany) and bovine skin collagen (Collagen G, 4 mg/ml, Matrix Bioscience) at a ratio of 1:1. We then added 10% (vol/vol) sodium bicarbonate (23 mg/ml) and 10% (vol/vol) 10× DMEM (Gibco). We adjusted the solution to pH 10 with 43 μl of 1 M NaOH and polymerized it at 37 °C, 95% humidity and 5% CO₂ for 1 h. For final collagen concentrations of 1.2 mg/ml and 0.6 mg/ml, we diluted the solution before polymerization with a mixture of 1 volume part NaHCO₃, 1 part 10× DMEM and 8 parts H₂O. We polymerized fibrin gels with a final concentration of 4.0 mg/ml human fibrinogen after mixing with 0.05 NIH units/ml human α-thrombin (both from Haemochrome Diagnostics) in buffer containing 0.15 M NaCl, 20 mM CaCl₂, 25 mM HEPES at pH 7.4 for 1 h at room temperature. We polymerized Matrigel (BD Bioscience) at a concentration of 10 mg/ml (undiluted) at 37 °C, 5% CO₂ and 95% relative humidity for 1 h.

Mechanical description of collagen gels. We assumed that the collagen network deforms in an affine way beyond a certain length scale, and that below that scale, individual fiber segments deform in a non-affine way and evade mechanical stress using their internal degrees of freedom (Fig. 1d). This can be described by a nonlinear and asymmetric energy potential function $w(\lambda) = w(\Delta l/l)$ of the fibers. The potential function $w(\lambda)$ of individual collagen fibers is expected to exhibit three distinct regimes: buckling, straightening and stretching. The differential fiber stiffness $w''(\lambda)$ can thus be described with only four parameters: (i) a buckling coefficient d_0 describing an exponential decrease in fiber stiffness under compression, (ii) linear stiffness κ_0 , (iii) critical strain for the onset of strain stiffening λ_s and (iv) an exponential strain stiffening coefficient d_s (Fig. 1d,e).

$$w''(\lambda) = \kappa_0 \begin{cases} e^{\lambda/d_0} & \forall \lambda < 0 \\ 1 & \forall 0 < \lambda < \lambda_s \\ e^{(\lambda - \lambda_s)/d_s} & \forall \lambda_s < \lambda \end{cases} \quad (1)$$

With a mean field approach, the deformation λ of a fiber is defined by the change in length Δl relative to the fiber's end-to-end distance in the unstressed state, $\lambda = \Delta l/l$. The value of λ is determined by the fiber displacement field \vec{U} and the local average deformation field $F = \text{grad } \vec{U}$ according to

$$\lambda = |F\vec{e}_\Omega| - 1 \quad (2)$$

with unit vector \vec{e}_Ω pointing in the direction of the fiber orientation Ω . The mechanical stress of the fiber is then

$$w'(\lambda) = \int_0^\lambda w''(\lambda) d\lambda$$

Integration from zero implies that the material has no pre-stress. One can derive a constitutive equation that relates the nominal stress tensor N to the deformation field F by averaging the stress contributions of many fibers, assuming an isotropic and homogeneous distribution¹² (Supplementary Note 2).

$$N_{ij} = \left\langle w'(|F\vec{e}_\Omega| - 1) \frac{(F\vec{e}_\Omega)_i \cdot (\vec{e}_\Omega)_j}{|F\vec{e}_\Omega|} \right\rangle_\Omega \quad (3)$$

Rheometer experiment. We used a cone-plate rheometer to measure the stress-strain relationship of collagen gels for simple shear deformation. The collagen was polymerized inside the rheometer setup. The cone-plate rheometer applied a simple shear deformation such that the strain energy density depended only on the engineering shear strain. We obtained the linear stiffness κ_0 , the stiffening coefficient d_s and the characteristic strain λ_s at the onset of stiffening by minimizing the error between the measured and computed stress-strain relationships (Supplementary Note 4).

Uniaxial stretch experiment. We cast collagen gel, fibrin gel or Matrigel into a flexible polydimethylsiloxane dish with a sulfosuccinimidyl 6-(4'-azido-2'-nitrophenylamino) hexanoate) activated surface. After polymerization, the gel in the dish was stretched uniaxially at a rate of 6% per hour with a stepper-motor device³³, and the height of the gel as a function of applied stretch was measured with a microscope³⁴. We fit the buckling coefficient d_0 of our constitutive equation (equation (3)) to best match the measured relationship of vertical versus horizontal strain. We took the other three material parameters of the constitutive equation from the shear rheometer experiment (Supplementary Note 4) in the case of collagen and from extensional rheometer experiments in the cases of fibrin and Matrigel.

The vertical contraction of a gel under horizontal stretching can be converted to an apparent Poisson's ratio, which in the case of collagen is considerably greater than 1. According to linear elastic theory, a Poisson's ratio of >0.5 leads to a negative bulk modulus, implying that the undeformed configuration of the material is unstable. The Poisson's ratio of a hydrogel, however, is that of the composite material, which in the case of a collagen gel consists of collagen fibers and water. When a collagen gel is stretched, water can be released. Moreover, the apparent Poisson's ratio of a collagen gel is highly asymmetric and nonlinear. For compression, the apparent Poisson's ratio is much less than 0.5 (Fig. 1b).

Extensional rheometer. For measuring the stress-strain relationship under uniaxial stretch, a cylinder of collagen, fibrin or Matrigel was cast between two parallel plates (diameter, 5 cm; gap, 3 mm) (Fig. 2a). The lower plate was connected to a precision scale (AND GR-200), and the upper plate was mounted on a motorized micromanipulator (Eppendorf Injectman). The gel was extended at a rate of 10 μm/s, and the weight was continuously recorded. The force-extension curve of the gel was corrected for the mechanical compliance of the device. The stress-strain relationship was computed from the corrected force-extension curve and the known geometry of the gel cylinder. The material parameters were then obtained as described for the shear rheometer experiment (Supplementary Note 4).

Finite-element method. To solve the constitutive equation (equation (3)) for arbitrary geometries and boundary conditions, we used a finite-element method in which the material was represented by a mesh of mechanically coupled tetrahedra. Given a set of displacements of the nodes (cornerpoints of the tetrahedra), we calculated the nodal forces as the derivative of the total strain energy of the material by the displacements of the respective nodes (Supplementary Note 2). In the case of a point-like

force applied to the surface of a gel, the mesh also included the free top surface. All other boundaries were fixed. The considered gel region around a cell was larger than 480 μm .

Magnetic-tweezers experiment. We measured the material displacement field in response to a point-like force at the surface by applying a lateral force of 10–30 nN to a superparamagnetic bead (Microparticles Berlin, Germany; diameter, 5 μm) with magnetic tweezers^{5,35}. The gel was decorated with 1- μm fluorescent beads (FluoSpheres, Molecular Probes) that served as fiducial markers. A stack of images around the magnetic bead was acquired before and 10 min after the onset of force application. The displacement of each fluorescent marker was then obtained from the image data as described in ref. 5. The measured displacements were interpolated to a regular finite-element mesh with a grid constant of 7.5 μm in the case of unconstrained force reconstruction, or to an irregular mesh with increasing mesh density near the magnetic bead in the case of constrained (point-like) force reconstruction. The coefficient of variation (CV) of the bead radius was ~5% as stated by the manufacturer, which led to an error (CV) of the applied force of 15%.

Constrained force reconstruction through direct fitting. Given a set of measured displacements of fluorescent markers inside a gel, we minimized the mismatch between the simulated and the measured gel displacements by shifting the location of force application in the simulation, as well as by adjusting the force amplitude and direction. The simulated displacement fields were calculated for a discrete set of force amplitudes and were linearly interpolated between these discrete solutions. The simulated displacement field was shifted, rotated and interpolated onto the positions of the fluorescent markers for which the displacement was measured. We then minimized the least-square error by randomly varying the shift, rotation and amplitude parameters until convergence was reached.

Cell culture. Cells were cultured in 25-cm² flasks without surface coating in DMEM (1 g/l D-glucose) with 10% FBS, 1% penicillin and streptomycin at 37 °C, 5% CO₂ and 95% humidity. Cells were passaged every 3 d. Trypsin-EDTA was used to detach cells. Cells were mixed with collagen solution before polymerization at a concentration of 15,000 cells/ml and incubated for 12 h before experiments. MDA-MB-231 breast carcinoma cells were obtained from ATTC; dual-color H2B-GFP/cytoplasmic TagRFP HT1080 fibrosarcoma cells were a gift from Katarina Wolf and were generated by Esther Wagena (Radboud University Nijmegen). All cell lines were checked with a mycoplasma PCR detection kit (Minerva Biolabs).

Fiber-pattern matching. To measure the displacement field of the matrix surrounding the cells, we imaged the collagen network directly using confocal reflection microscopy (Leica SP5X, 20 \times dip-in water-immersion objective (numerical aperture (NA) 1.0)). Confocal reflection microscopy needs only low laser intensities and prevents photodamage of the cells. From two stacks of confocal reflection images (voxel size of 0.72 μm in all dimensions, field of view of 370 μm in all dimensions) that were taken before and after cell force relaxation with cytochalasin D, we obtained the cell-induced deformation field over a regular grid with

a 7.5- μm mesh size by particle image velocimetry as follows. The algorithm we used calculated the cross-correlation between corresponding local sections (12 \times 12 \times 12 voxels) of the two stacks. It then shifted the section of the first stack by subvoxel increments using trilinear interpolation. This shift corresponded to a displacement vector. To find the local displacement with the highest cross-correlation, we used the downhill simplex method³⁶. The accuracy of the deformation measurements was 60 nm (r.m.s.) (Supplementary Note 12). For 1.2-mg/ml gels with an average pore size of 3.8 μm , the optimal mesh size of the gel subvolumes used for cross-correlation, and thus the spatial resolution of the algorithm, was 7.5 μm (Supplementary Note 12).

Force reconstruction. We reconstructed the 3D force field (force per volume) inside a continuous material, assuming that cellular forces could exist everywhere inside the considered volume. This left us with a computational problem, as the number of fitted parameters (force vectors) equaled the number of data points (measured displacement vectors). We therefore used a regularization method. We performed regularization by minimizing a target function (\underline{u}) that was the sum of the ordinary least-square displacement error and a locally weighted norm of the nodal forces.

$$L(\underline{u}) = \left\| \underline{u} - \underline{u}_{\text{measured}} \right\|_{\underline{P}}^2 + \left\| \underline{f}(\underline{u}) \right\|_{\underline{A}}^2$$

where $\left\| \underline{x} \right\|_{\underline{Q}}$ denotes $\underline{x}^T \underline{Q} \underline{x}$. The diagonal matrix \underline{P} has a value of 1 if the displacement of the corresponding node is known and a value of 0 if the displacement reconstruction algorithm is not able to measure the local displacement, or if the corresponding node lies outside of the imaged section. The matrix \underline{A} is a diagonal matrix containing the local penalty weights. If \underline{A} is proportional to the identity matrix (this corresponds to the Tikhonov regularization method), all nodal forces are penalized and therefore underestimated. To address this issue, we used the maximum-likelihood regression method, which iteratively assigns a lower penalty weight to nodes that have a high force³⁷.

$$A_{ii} = \begin{cases} \alpha, & |f_i| < 1.345 \cdot \text{median}(|\underline{f}|) \\ \frac{\alpha \cdot 1.345 \cdot \text{median}(|\underline{f}|)}{|f_i|}, & |f_i| > 1.345 \cdot \text{median}(|\underline{f}|) \end{cases}$$

This procedure reliably penalizes forces due to uncorrelated displacement noise but not cell forces, which are accompanied by long-ranging and correlated displacements. Thus, the algorithm finds the cell forces in an unconstrained manner. It is also possible to constrain the forces to the surface of the cell by predefining low or zero values for the local-penalty-weight matrix \underline{A} at specific points corresponding to the cell surface (Supplementary Note 18).

The locally weighted norm of the nodal forces, $\left\| \underline{f}(\underline{u}) \right\|_{\underline{A}}^2$, is nonlinear in \underline{u} , and therefore $L(\underline{u})$ cannot be easily minimized. We expanded $\underline{f}(\underline{u})$ as a first-order Taylor series for nodal displacements $\underline{u} + \underline{\Delta u}$ (Supplementary Note 9), using the stiffness tensor \underline{K} (Supplementary Note 3).

$$L(\underline{u} + \underline{\Delta u}) = \left\| \underline{u} + \underline{\Delta u} - \underline{u}_{\text{measured}} \right\|_{\underline{P}}^2 + \left\| \underline{f}_{\underline{u}} + \underline{K}_{\underline{u}} \cdot \underline{\Delta u} \right\|_{\underline{A}}^2$$

To find the value of $\underline{\Delta u}$ that minimized this expression, we solved the following equation using the conjugate gradient method³⁸:

$$(\underline{P} + \underline{K}_u \cdot \underline{A} \cdot \underline{K}_u) \cdot \underline{\Delta u} = \underline{P} \cdot (u_{\text{measured}} - u) - \underline{K}_u \cdot \underline{A} \cdot f_u$$

We then added $\underline{\Delta u}$ to the estimated nodal displacements u and updated the Taylor coefficients f_u and \underline{K}_u and the local weight matrix \underline{A} for the next iteration until convergence was reached.

To compute the total contractility of a cell without bias caused by noise forces from regions outside the cell, we computed for every node \vec{r}_n of the gel the contractile force C_{tot} as the scalar product of the force at that node with a unit vector pointing toward the cell force center \vec{r}_c (ref. 39) (**Supplementary Note 13**).

The source code of the algorithm, including the 3D particle image velocimetry and the unconstrained force reconstruction, is available under MIT license on the collaborative coding platform GitHub (<https://github.com/Tschaul/SAENO>) and is free to download. A compiled version of the software and a tutorial are provided as **Supplementary Software**, together with a sample data set (<http://lpmt.biomed.uni-erlangen.de/3DTractions/SampleData.rar>).

Analysis of cell migration. We extracted the center-of-mass movement of the cells from their brightfield projections.

The movement of the center of mass is described as a persistent random motion with time-varying migratory activity and migratory persistence. We extracted the time courses of both of these parameters from the measured trajectories using a Bayesian method of sequential inference²⁸. Only cells that were not undergoing cell division during measurements were included in the correlation analysis.

Statistical analysis. Differences between measurements were considered statistically significant at $P < 0.05$ by Student's two-tailed t -test assuming unequal variances.

33. Bonakdar, N. *et al.* Biomechanical characterization of a desminopathy in primary human myoblasts. *Biochem. Biophys. Res. Commun.* **419**, 703–707 (2012).
34. Faust, U. *et al.* Cyclic stress at mHz frequencies aligns fibroblasts in direction of zero strain. *PLoS ONE* **6**, e28963 (2011).
35. Kollmannsberger, P. & Fabry, B. High-force magnetic tweezers with force feedback for biological applications. *Rev. Sci. Instrum.* **78**, 114301 (2007).
36. Nelder, J.A. & Mead, R. A simplex method for function minimization. *Comput. J.* **7**, 308–313 (1965).
37. Huber, P.J. *Robust Statistics* (John Wiley & Sons, 1981).
38. Tikhonov, A.N. Solution of incorrectly formulated problems and the regularization method. *Soviet Mathematics Doklady* **4**, 1035–1038 (1963).
39. Hersch, N. *et al.* The constant beat: cardiomyocytes adapt their forces by equal contraction upon environmental stiffening. *Biol. Open* **2**, 351–361 (2013).

Supplementary Notes - Three-dimensional Force Microscopy of Cells in Biopolymer Networks

*J. Steinwachs, C. Metzner, K. Skodzek, N. Lang,
I. Thievensen, C. Mark, S. Münster, K. Aifantis, B. Fabry*

October 22, 2015

Note 1 Stiffness tensor of a semi-affine material

The stiffness tensor is defined as the derivative of the nominal stress by the deformation gradient.

$$K_{ijkl} = \frac{\partial N_{ij}}{\partial F_{kl}}$$

In a linear material, the stiffness tensor is independent of the deformation state of the material. Since our constitutive equation is non-linear, however, the stiffness tensor depends on the deformation. Differentiation of Eq. 3 (main text) gives

$$K_{ijkl} = \frac{\partial N_{ij}}{\partial F_{kl}} = \left\langle e_{\Omega i} \cdot e_{\Omega k} \cdot \left(\frac{|\mathbf{F} \cdot \vec{e}_{\Omega}| \cdot w''(|\mathbf{F} \cdot \vec{e}_{\Omega}| - 1) - w'(|\mathbf{F} \cdot \vec{e}_{\Omega}| - 1)}{|\mathbf{F} \cdot \vec{e}_{\Omega}|^2} \right. \right. \quad (1)$$

$$\left. \left. \frac{(\mathbf{F} \cdot \vec{e}_{\Omega})_j \cdot (\mathbf{F} \cdot \vec{e}_{\Omega})_l}{|\mathbf{F} \cdot \vec{e}_{\Omega}|} + \frac{w'(|\mathbf{F} \cdot \vec{e}_{\Omega}| - 1)}{|\mathbf{F} \cdot \vec{e}_{\Omega}|} \cdot \delta_{jl} \right) \right\rangle_{\Omega}; \quad k \in \{x, y, z\}; \quad l \in \{x, y, z\}$$

This exact expression of the stiffness tensor is used further below for the traction force reconstruction in a non-linear material. For readers who are interested to know how this stiffness tensor is related to the more familiar description of mechanical properties in the framework of linear elastic theory, we provide the following explanation. In linear elastic theory, the stiffness of a material is fully defined by two parameters, for example the Young's modulus (Y) and the Poisson's ratio (ν). To relate the 4 parameters of our constitutive equation to Y and ν , we approximate the stiffness tensor \mathbf{K} for small strain ($\mathbf{F} \approx \mathbf{I}$). In this case, the fiber stretch λ is 0 for all solid angles $[\theta, \phi] = \Omega$, which yields the following simplifications:

$$w(\lambda) = 0; \quad w'(\lambda) = 0; \quad w''(\lambda) = \kappa_0;$$

We can therefore rewrite the stiffness tensor

$$K_{ijkl}(\mathbf{F} = \mathbf{I}) = \kappa_0 \cdot \langle e_{\Omega i} \cdot e_{\Omega k} \cdot e_{\Omega j} \cdot e_{\Omega l} \rangle_{\Omega}$$

The stiffness for extension, as measured in our extensional rheometer experiments, therefore can be expressed as a function of Y and ν [ZienkiewiczV1 page 132]

$$K_{zzzz}(\mathbf{F} = \mathbf{I}) = \frac{1}{4\pi} \cdot \kappa_0 \cdot \iint \cos(\theta)^4 d\Omega = \frac{\kappa_0}{5} = \frac{Y \cdot (1 - \nu)}{(1 + \nu)(1 - 2\nu)} \quad (2)$$

Similarly, the stiffness perpendicular to the stretch direction is given by

$$K_{zzyy}(\mathbf{F} = \mathbf{I}) = \frac{1}{4\pi} \cdot \kappa_0 \cdot \iint \cos(\theta)^2 \cdot \sin(\theta)^2 \cdot \sin(\phi)^2 d\Omega = \frac{\kappa_0}{15} = \frac{Y \cdot \nu}{(1 + \nu)(1 - 2\nu)}$$

Together, it follows that

$$Y = \frac{\kappa_0}{6} \text{ and } \nu = 0.25 \quad (3)$$

As described below, we experimentally confirm a Poisson's ratio of $\nu = 0.25$ for a linear elastic biopolymer network such as Matrigel.

Note 2 Hyperelastic finite element method

The finite element method is used to numerically compute solutions to mechanical boundary value problems. In most applications, linear materials are considered. To solve boundary value problems imposed by a contracting cell embedded in a collagen biopolymer network, however, we need a fully hyperelastic finite element model. The geometry of the material, in this case the collagen gel, is discretized into multiple tetrahedral elements, which together fill the entire space of the material. Neighboring elements share one or more of their corner points. The displacement field inside the material is discretized to these corner points (the nodes) and linearly interpolated inside the tetrahedra. Because of this linear interpolation, the deformation gradient (\mathbf{F}) is constant over the volume of a tetrahedron. The deformation gradient is the linear map of the undeformed tetrahedron T onto the deformed tetrahedron T' [Ogden page 84].

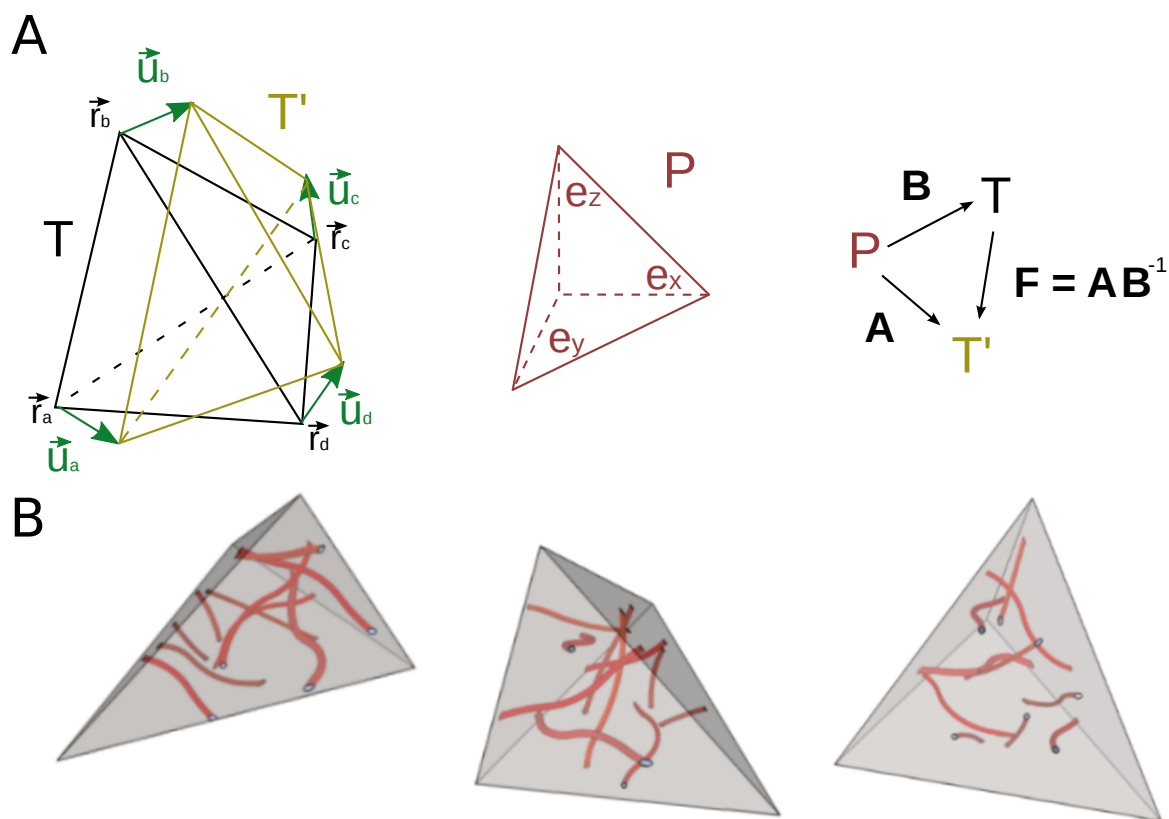


Figure S 1: (A) A tetrahedron $T \triangleq [r_a, r_b, r_c, r_d]$ is deformed by displacements u_a, u_b, u_c and u_d at its corner points. The primitive tetrahedron P has three of its edges aligned with the coordinate axes e_x, e_y and e_z . Linear maps (\mathbf{B} and \mathbf{A}) of P onto T as well as T' are straight forward to compute. The linear map \mathbf{F} of T onto T' is then simply given by $\mathbf{A} \cdot \mathbf{B}^{-1}$. (B) Tetrahedral elements of the finite element model are filled with fiber elements, and the stresses at the faces of each tetrahedron are computed by averaging the individual forces of the intersecting fibers.

Next, we need to find the matrix \mathbf{B} that describes the linear map of the undeformed tetrahedron T onto the primitive tetrahedron P that is defined by corner points $[(0, 0, 0) (1, 0, 0) (0, 1, 0) (0, 0, 1)]$ (Fig. S 1). \mathbf{B} is given by the matrix with the vectors $(r_b - r_a)$, $(r_c - r_a)$ and $(r_d - r_a)$ as column vectors. We also need the matrix \mathbf{A} that describes the linear map of P onto the deformed tetrahedron T' . It is given by the matrix with the vectors $(r_b - r_a + u_b - u_a)$, $(r_c - r_a + u_c - u_a)$ and $(r_d - r_a + u_d - u_a)$ as column vectors. The linear map \mathbf{F} that maps T to T' is then given by $\mathbf{A} \cdot \mathbf{B}^{-1}$. Using the 4x3 helper tensor

$$\mathcal{X}_{mk} = \begin{matrix} & x & y & z \\ a & -1 & -1 & -1 \\ b & 1 & 0 & 0 \\ c & 0 & 1 & 0 \\ d & 0 & 0 & 1 \end{matrix}$$

and using Einstein notation, the deformation gradient matrix \mathbf{F} can be rewritten as a function of the nodal displacements u_m :

$$A_{ij} = B_{ij} + u_{mi} \cdot \mathcal{X}_{mj}; \quad m \in \{a, b, c, d\}; \quad i \in \{x, y, z\}; \quad j \in \{x, y, z\}$$

$$\begin{aligned}
F_{ij} &= B_{ik} \cdot B_{kj}^{-1} + u_{mi} \cdot \mathcal{X}_{mk} \cdot B_{kj}^{-1}, \quad k \in \{x, y, z\} \\
&= \delta_{ij} + u_{mi} \cdot \underbrace{\mathcal{X}_{mk} \cdot B_{kj}^{-1}}_{\Phi_{mj}}
\end{aligned}$$

where Φ is the shape tensor of the tetrahedron and δ_{ij} is the Kronecker delta. The derivative of \mathbf{F} with respect to the displacements u_m , which when multiplied with the stress tensor \mathbf{N} gives the nodal forces $\frac{\partial E_T}{\partial u_{ml}}$ of the tetrahedron T (E_T denotes the strain energy of the tetrahedron T), is then given by

$$\frac{\partial F_{ij}}{\partial u_{mk}} = \delta_{ik} \cdot \mathcal{X}_{mn} \cdot B_{nj}^{-1} = \delta_{ik} \cdot \Phi_{mj} \quad (4)$$

$$\frac{\partial E_T}{\partial u_{ml}} = V_T \cdot \frac{\partial W_T}{\partial F_{ij}} \frac{\partial F_{ij}}{\partial u_{ml}} = V_T \cdot N_{Tlj} \cdot \Phi_{mj} \quad (5)$$

Next, the equilibrium condition (Cauchy's law of motion) is formulated for a tetrahedral mesh. This is done by applying the principle of virtual work, which states that a deformation is a solution to a given boundary value problem if and only if the variation of the potential energy vanishes for all admissible small variations of the deformation $\delta \vec{u}$. [Ogden page 312]

Below, we solve the boundary value problem of imposed displacements and tractions for a single tetrahedron $T \triangleq [r_a, r_b, r_c, r_d]$. The faces of the tetrahedron are indexed in the following way:

$$\begin{aligned}
\alpha &\triangleq [r_b, r_c, r_d] \\
\beta &\triangleq [r_c, r_d, r_a] \\
\gamma &\triangleq [r_a, r_b, r_d] \\
\delta &\triangleq [r_a, r_b, r_c]
\end{aligned} \quad (6)$$

$$l \in \{\alpha, \beta, \gamma, \delta\}$$

A_{Tl} denotes the surface area of the face l of the tetrahedron T . The surface traction at a given set of faces $\{l\}$ is t_{Tl} . Further, only a subset of the corner points of the tetrahedron $\{d\} \subset \{m\}$ is free to move, and a constant body force b_T (e.g. an external force from the cell or a magnetic bead) is acting on the tetrahedron with volume V_T and density ρ_0 . We can write the variation of the potential energy as [Ogden page 308]

$$\int_{V_T} \delta W \, dV - \int_{V_T} \rho_0 b_T \cdot \delta \vec{u} \, dV - \int_{A_{\{l\}}} t_{Tl} \cdot \delta \vec{u} \, dA = 0 \quad (7)$$

Here, $\delta \vec{u}$ are small variations to the displacements of the tetrahedron. The first term is the variation of the total strain energy inside the tetrahedron. The strain energy density is a function of the deformation gradient and is constant over the tetrahedron. We therefore rewrite the first term as a function of the variation of the displacements at the corner points δu_m .

$$\int_{V_T} \delta W \, dV = V_T \cdot \frac{\partial W_T}{\partial F_{Tij}} \frac{\partial F_{Tij}}{\partial u_{mk}} \delta u_{mk} = \frac{\partial E_T}{\partial u_{mk}} \delta u_{mk} \quad (8)$$

In the second term of Eq. S 7, the variation of the displacements are averaged over the volume and multiplied with the body force. The second term can therefore be expressed as the arithmetic mean of the variation of the displacements at the 4 corner points.

$$\int_{V_T} \rho_0 \vec{b} \cdot \delta \vec{u} dV = \rho_0 \cdot V_T \cdot b_{Tk} \cdot \frac{1}{4} \delta u_{mk} \quad (9)$$

Finally, in the third term of Eq. S 7, the variation of the displacements are averaged separately over the faces, which are subject to boundary tractions. The average surface displacements \bar{u}_{lk} are given by the arithmetic mean of the 3 displacements of the corner points framing the face of the tetrahedron. With the definition of the face index (Eq. S 6), we can derive the helper tensor

$$h_{lm} = \frac{\partial \bar{u}_l}{\partial u_m} = \begin{matrix} & & a & b & c & d \\ \alpha & \left[\begin{array}{cccc} 0 & \frac{1}{3} & \frac{1}{3} & \frac{1}{3} \\ \frac{1}{3} & 0 & \frac{1}{3} & \frac{1}{3} \\ \frac{1}{3} & \frac{1}{3} & 0 & \frac{1}{3} \\ \frac{1}{3} & \frac{1}{3} & \frac{1}{3} & 0 \end{array} \right] \\ \beta & \\ \gamma & \\ \delta & \end{matrix} \quad (10)$$

$m \in \{\text{corner points of the tetrahedron: } a, b, c, d\}; l \in \{\text{faces of the tetrahedron: } \alpha, \beta, \gamma, \delta\}$

and write

$$\int_{A_{T\{l\}}} \vec{t}_l \cdot \delta \vec{u} dA = t_{Tlk} \cdot h_{lm} \cdot A_{Tl} \cdot \delta u_{mk} \quad (11)$$

Summing up all three terms, we can rewrite the variation of the potential energy and then factor out the variation of the displacements at the corner points $\delta \vec{u}_m$:

$$\begin{aligned} \frac{\partial E_T}{\partial u_{mk}} \delta u_{mk} - \rho_0 \cdot V_T \cdot b_k \cdot \frac{1}{4} \delta u_{mk} - t_{Tlk} \cdot h_{lm} \cdot A_{Tl} \cdot \delta u_{mk} &= 0 \\ = \delta u_{mk} \cdot \left(\frac{\partial E_T}{\partial u_{mk}} - \rho_0 \cdot V_T \cdot b_{Tk} \cdot \frac{1}{4} - t_{Tlk} \cdot h_{lm} \cdot A_{Tl} \right); & \quad k \in \{x, y, z\} \end{aligned}$$

For the fixed nodes, the variation of the displacements are zero. Therefore, we sum only over the free corner of the tetrahedron, d instead of m .

$$\delta u_{dk} \cdot \left(\frac{\partial E_T}{\partial u_{dk}} - \rho_0 \cdot V_T \cdot b_{Tk} \cdot \frac{1}{4} - t_{Tlk} \cdot h_{ld} \cdot A_{Tl} \right) = 0; d \in \{\text{free corner points of the tetrahedron}\}$$

Since this equation has to hold for all possible variations of the displacements, the term in the brackets must be zero.

$$\frac{\partial E_T}{\partial u_{dk}} - \frac{\rho_0}{4} \cdot V_T \cdot b_{Tk} - t_{Tlk} \cdot h_{ld} \cdot A_{Tl} = 0 \quad (12)$$

In order to extend this equation to multiple connected tetrahedra, we sum over multiple tetrahedra. All arguments keep their meaning so that we can apply the summation directly to (Eq. S 12) using the helper tensor θ :

$$\theta_{Tom} = \begin{cases} 1, & \text{if the node } o \text{ is the corner point } m \text{ of the tetrahedron } T \\ 0, & \text{else} \end{cases} \quad (13)$$

Again, we only sum over free nodes of the tetrahedral mesh:

$$\theta_{T_{om}} \cdot \left(\frac{\partial E_T}{\partial u_{mk}} - \frac{\rho_0}{4} \cdot V_T \cdot b_{Tk} - t_{Tlk} \cdot h_{lm} \cdot A_{Tl} \right) = 0; \quad o \in \{\text{free nodes}\}$$

We can rewrite this as a differential equation of the total strain energy of the body $E = \sum_T E_T$.

$$(\underline{f}_u)_{ok} = \frac{\partial E}{\partial u_{ok}} = \theta_{T_{om}} \cdot \left(\frac{\rho_0}{4} \cdot V_T \cdot b_{Tk} + t_{Tlk} \cdot h_{lm} \cdot A_{Tl} \right) = -(\underline{f}_{ext})_{ok} \quad (14)$$

with \underline{f}_{ext} denoting the external nodal forces. Therefore, the body is in equilibrium if the internal nodal forces \underline{f}_u counterbalance the external nodal forces, which can be calculated for any boundary value problem using Eq. S 14. In reverse, Eq. S 14 can be used to calculate the body forces, which describe external forces from a cell or a magnetic bead, given a set of nodal forces \underline{f}_u as retrieved from the unconstrained force reconstruction algorithm.

Note 3 Discretization of the semi-affine elastic network model for tetrahedral meshes

In our semi-affine elastic network description, the strain energy density is given by.

$$W = \langle w(|\mathbf{F} \cdot \vec{e}_r(\Omega)| - 1) \rangle_{\Omega} \quad (15)$$

To make it numerically accessible, the averaging over the solid angle Ω is substituted by averaging over a finite set of N_b angles Ω_b that are isotropically distributed. We use the notation:

$$\vec{s}_b = \vec{e}_r(\Omega_b)$$

$$\vec{s}_b^T = \mathbf{F}_T \cdot \vec{s}_b$$

The integration over the material volume is substituted by a summation over the volumes of tetrahedra T that fill the space of the body (see previous section). With that, the strain energy is:

$$E_T = \frac{1}{N_b} \sum_b w(|\vec{s}_b^T| - 1) \cdot V_T$$

$$E = \sum_T E_T$$

E_T is the energy stored inside the tetrahedron T . V_T is the volume of the tetrahedron T . The nodal forces \underline{f}_u (Eq. S 14) are defined as the derivatives of the total energy with respect to the nodal displacements \vec{u}_t . In the following, we use the helper tensor θ (Eq. S 13).

$$(\underline{f}_u)_{ol} = \frac{\partial E}{\partial u_{ol}} = \sum_T \sum_m \theta_{T_{om}} \cdot \frac{\partial E_T}{\partial u_{ml}}; \quad T \in \{\text{tetrahedra}\}; \quad o \in \{\text{nodes}\}; \quad m \in \{a, b, c, d\}; \quad l \in \{x, y, z\} \quad (16)$$

Here, $\frac{\partial E_T}{\partial u_{ml}}$ are the nodal forces of the tetrahedron T .

$$\frac{\partial E_T}{\partial u_{ml}} = \frac{1}{N_b} \cdot V_T \cdot \sum_b \underbrace{\frac{\partial w(|\vec{s}'_b| - 1)}{\partial |\vec{s}'_b|}}_{w'(|\vec{s}'_b| - 1)} \cdot \underbrace{\frac{\partial |\vec{s}'_b|}{\partial F_{ij}}}_{\frac{s'_{bi} \cdot s_{bj}}{|\vec{s}'_b|}} \cdot \frac{\partial F_{ij}}{\partial u_{ml}}$$

Using (Eq. S 4) we obtain:

$$\frac{\partial E_T}{\partial u_{ml}} = \frac{1}{N_b} \cdot \sum_b w'(|\vec{s}'_b| - 1) \cdot \frac{s'_{bi} \cdot s_{bj}}{|\vec{s}'_b|} \cdot \delta_{il} \cdot \Phi_{mj} = \frac{1}{N_b} \cdot \sum_b \frac{w'(|\vec{s}'_b| - 1)}{|\vec{s}'_b|} \cdot s'_{bl} \cdot \underbrace{\Phi_{mj} \cdot s_{bj}}_{(\Phi \cdot \vec{s}'_b)_m = s_{bm}^*}$$

Finally, the stiffness of the tetrahedral mesh $\underline{\underline{K_u}}$ can be derived.

$$\begin{aligned} \left(\underline{\underline{K_u}}\right)_{olpi} &= \frac{\partial^2 E}{\partial u_{ol} \partial u_{pi}} = \sum_T \sum_r \sum_m \theta_{T om} \cdot \theta_{T pr} \cdot \frac{\partial^2 E_T}{\partial u_{ml} \partial u_{ri}} ; r \in \{a, b, c, d\}; p \in \{\text{nodes}\}; i \in \{x, y, z\} \quad (17) \\ &= \frac{\partial^2 E_T}{\partial u_{ml} \partial u_{ri}} = \frac{\partial}{\partial u_{ri}} \left(\frac{1}{N_b} \sum_b \frac{w'(|\vec{s}'_b| - 1)}{|\vec{s}'_b|} \cdot s'_{bl} \cdot s_{bm}^* \right) \\ &= \frac{1}{N_b} \sum_b s_{bm}^* \cdot \left(\frac{\partial}{\partial |\vec{s}'_b|} \left(\frac{w'(|\vec{s}'_b| - 1)}{|\vec{s}'_b|} \right) \cdot \frac{\partial |\vec{s}'_b|}{\partial u_{ri}} \cdot s'_{bl} + \frac{w'(|\vec{s}'_b| - 1)}{|\vec{s}'_b|} \cdot \frac{\partial s'_{bl}}{\partial u_{ri}} \right) \\ &= \frac{1}{N_b} \sum_b s_{bm}^* \cdot s_{br}^* \cdot \left(\frac{|\vec{s}'_b| \cdot w''(|\vec{s}'_b| - 1) - w'(|\vec{s}'_b| - 1)}{|\vec{s}'_b|^2} \cdot \frac{s'_{bi} \cdot s'_{bl}}{|\vec{s}'_b|} + \frac{w'(|\vec{s}'_b| - 1)}{|\vec{s}'_b|} \cdot \delta_{li} \right) \end{aligned}$$

This can be reexpressed by the stiffness tensor \mathbf{K}

$$\frac{\partial^2 E_T}{\partial u_{ml} \partial u_{ri}} = \sum_{j,k} V_T \cdot K_{Tj l k i} \cdot \Phi_{mj} \cdot \Phi_{rk}$$

Note 4 Model fit to bulk rheology

To extract the four material parameters κ_0 , d_0 , λ_s and d_s from macrorheological measurements, we compute the response predicted by our constitutive equation and minimize the mismatch between data and prediction by varying the parameter values. Below, we describe how the model predictions are calculated for three different macrorheological experiments.

Note 4.1 Shear rheometer

The shear rheometer applies a simple shear deformation γ of the following form to the gel:

$$\mathbf{F}(\gamma) = \begin{pmatrix} 1 & \gamma & 0 \\ 0 & 1 & 0 \\ 0 & 0 & 1 \end{pmatrix}$$

The resulting stress is then given by the partial derivative of the strain energy density with respect to the engineering shear strain γ , which we compute numerically.

$$\sigma(\gamma) = \frac{dW(\mathbf{F}(\gamma))}{d\gamma} \quad (18)$$

Note 4.2 Extensional rheometer

The extensional rheometer applies a uniaxial strain ϵ of the following form to the gel:

$$\mathbf{F}(\epsilon) = \begin{pmatrix} \epsilon & 0 & 0 \\ 0 & 1 & 0 \\ 0 & 0 & 1 \end{pmatrix}$$

The resulting stress is then given by the partial derivative of the strain energy density with respect to the strain ϵ , which we compute numerically.

$$\sigma(\epsilon) = \frac{dW(\mathbf{F}(\epsilon))}{d\epsilon} \quad (19)$$

Note 4.3 Uniaxial stretch

In this experiment, the deformation of the gel is described by two parameters. With the stretching device, we impose a horizontal strain λ_h and then measure the vertical strain λ_v . The deformation gradient is given by

$$\mathbf{F}(\lambda_h, \lambda_v) = \begin{pmatrix} \lambda_h & 0 & 0 \\ 0 & 1 & 0 \\ 0 & 0 & \lambda_v \end{pmatrix}$$

$$\Rightarrow W(\mathbf{F}(\lambda_h, \lambda_v)) = W(\lambda_h, \lambda_v)$$

To compute λ_v , we minimize the strain energy density with respect to λ_h numerically.

$$\lambda_v(\lambda_h) = \operatorname{argmin}(W(\lambda_h, \lambda_v), \lambda_v) \quad (20)$$

Note 5 Concentration dependence of material parameters for collagen gels

We measure the strain-dependent Young's modulus as well as the vertical contraction as a function of the horizontal stretch for three different collagen concentrations (0.6, 1.2, and 2.4 mg/ml). By fitting our material model, we find that the Young's modulus increases with the concentration while all other parameters remain unchanged. This is in agreement with the notion that only the density of fibers increases with the collagen concentration, but that the internal mechanics of individual fibers does not change.

	Linear stiffness	Linear range	Strain stiffening coefficient	Buckling parameter
0.6 mg/ml	447 Pa	0.0075	0.033	0.0008
1.2 mg/ml	1645 Pa	0.0075	0.033	0.0008
2.4 mg/ml	5208 Pa	0.0075	0.033	0.0008

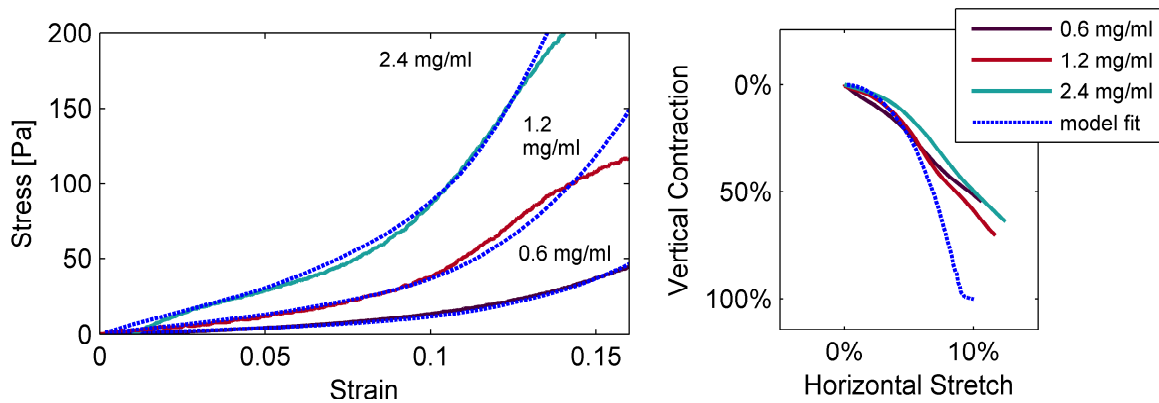


Figure S 2: Mechanical properties of collagen gels with different concentrations. **(Left)** Material stress as a function of uniaxial strain measured in an extensional rheometer for three different collagen concentrations (solid lines). With increasing concentration, the gel becomes stiffer. Blue lines indicates the semi-affine model fit to the data. **(Right)** Vertical contraction as a function of the horizontal stretch measured for three different collagen concentrations (solid lines) and model fit (dashed line). The collagen gels with different collagen concentrations do not show strong differences in their vertical to horizontal contraction ratio. Vertical contraction is not strongly affected by the collagen concentration. For principals strains (vertical contractions) above 40%, data and fit deviate due to batch dependent variations of the buckling parameter.

Note 6 Material parameters of a fibrin gel

In agreement with published data, from extensional rheometer and uniaxial stretch measurements, we find that fibrin shows no strain stiffening at small strain ($< 50\%$) but an abnormal Poisson's ratio [Brown 2009]. In our model, the strain stiffening depends on the response of the fibers under stretch, whereas the abnormal Poisson's ratio depends on the response of the fibers under compression. Hence, strain stiffening and vertical contraction under stretch are decoupled both in our model and in the data. During polymerization, fibrin gels form a dense but thin ($< 1\ \mu\text{m}$) scalelike skin at the surface. The mechanical stiffness of the skin layer is considerably higher than that of the fibrin bulk. Therefore, we were unable to verify our model under point-like forces with a magnetic tweezer.

	Linear stiffness	Linear range	Strain stiffening coefficient	Buckling parameter
4.0 mg/ml	2091 Pa	∞	∞	0.002

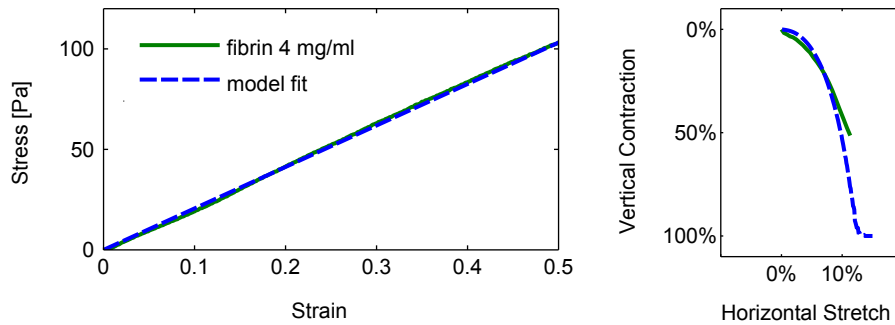


Figure S 3: Fibrin gels show vertical contraction due to fiber buckling but no strain stiffening for strains up to 50%. **(Left)** Material stress as a function of uniaxial strain measured in an extensional rheometer for a fibrin gels. We find a linear response for strains up to 50% **(Right)** Vertical contraction as a function of the horizontal stretch measured for a fibrin gel (solid lines) and the model fit (dashed line).

Note 7 Material parameters of Matrigel

For Matrigel (10 mg/ml, BD Bioscience, polymerized at 37 °C for 1 h), we find a constant strain-independent Young's modulus of 394 Pa and a constant vertical to horizontal contraction ratio of 0.34, which exactly matches the prediction for a material in which the fibers are linear in compression and extension and therefore do not buckle. In this case the Poisson's ratio is 0.25 (Eq. S 3). The semi-affine elastic network model predicts that the displacement field around a point-like force is also symmetric, in contrast to a material that shows buckling (Fig. 3 F+H, main text). This is in agreement with measurements where we record the displacement field around a magnetic bead that is laterally pulled with a force of 20 nN.

	Linear stiffness	Linear range	Strain stiffening coefficient	Buckling parameter
10 mg/ml	2364 Pa	∞	∞	∞

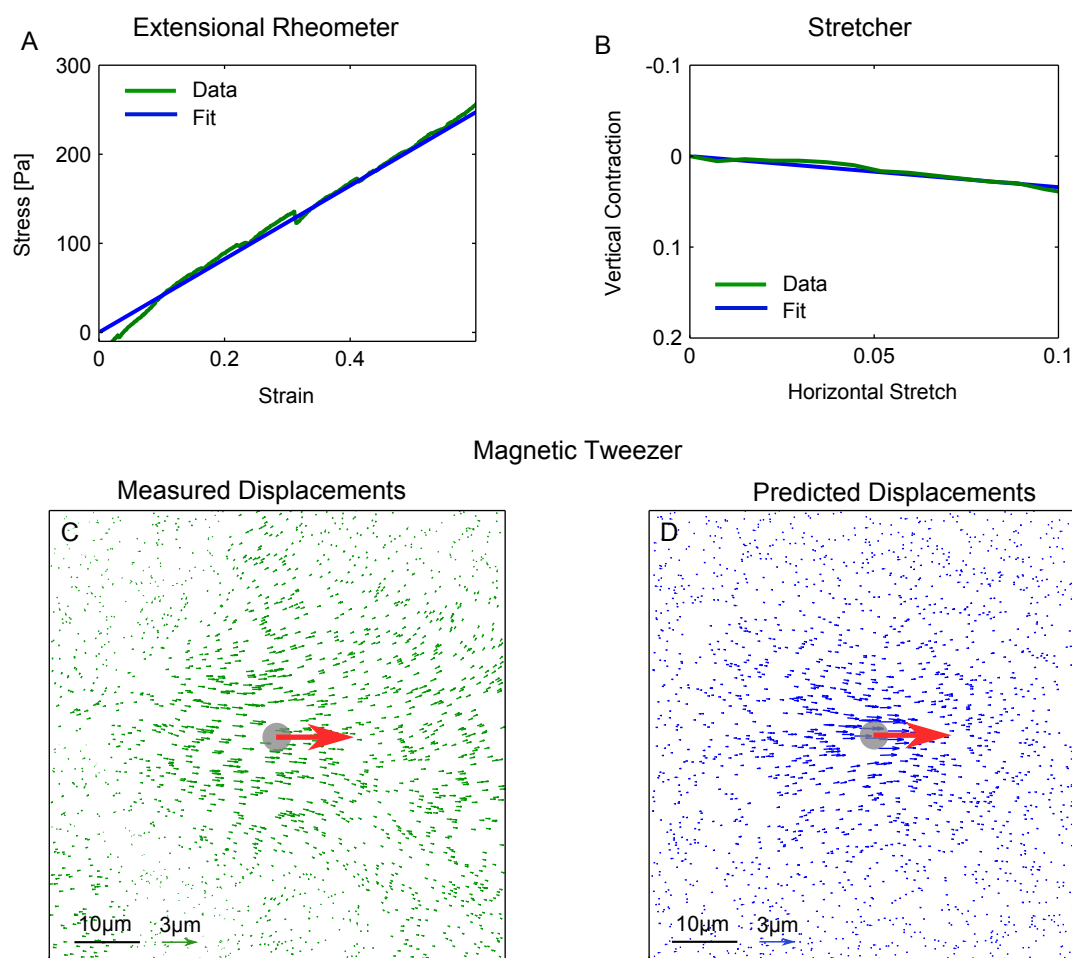


Figure S 4: Matrigel shows neither fiber buckling nor strain stiffening. **(A)** Material stress as a function of uniaxial strain measured in an extensional rheometer for Matrigel. We find a linear response for strains up to 50% **(B)** Vertical contraction as a function of the horizontal stretch measured for Matrigel (green) and model fit (blue). Matrigel shows a horizontal contraction ratio of 0.34, in agreement with the model prediction for fibers that do not buckle under compression. **(C)** The matrix displacement field around a magnetic bead to which we applied a force of 20 nN. **(D)** Model predictions for the displacement field agree with the measurements.

Note 8 Detailed influence of material parameters on bulk rheology

To investigate the influence of the material parameters (κ_0 , d_0 , d_s and λ_s) on different non-linear effects, we analyze how the predicted macrorheological behavior changes when we independently vary the four material parameters. We find that the buckling coefficient d_0 has the largest effect on the vertical contraction under horizontal stretch (Fig. S 5 B). By contrast, the stiffening coefficient d_s and especially the onset of fiber stiffening λ_s have only a minor effects on the vertical contraction under horizontal stretch (Fig. S 5 A,C). The linear stiffness under shear is solely determined by the linear fiber stiffness κ_0 (Fig. S 5 E). The degree of strain stiffening is determined mostly by d_s (Fig. S 5 D), and the onset of strain stiffening by λ_s (Fig. S 5 F). Thus, the fit parameters have a clear physical meaning and show only a small covariance, which makes the fit to the data robust.

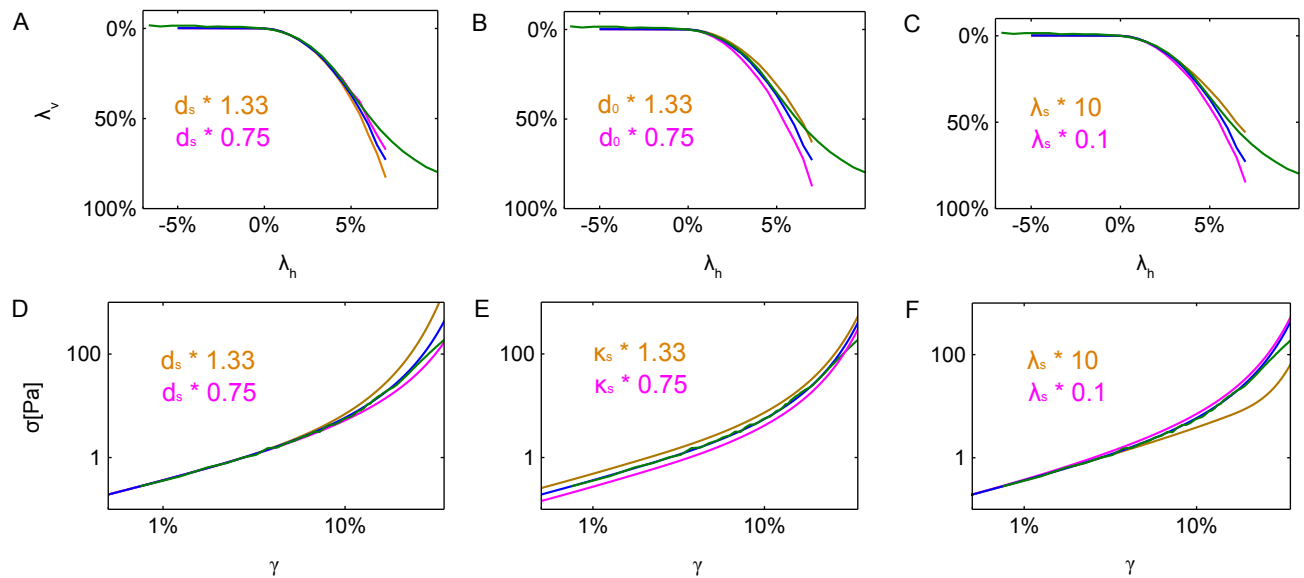


Figure S 5: Influence of model parameters on macrorheology. (A,B,C): Uniaxial stretch: Data in green, fit in blue, fit with altered parameters in pink and brown (D,E,F) Shear rheometer experiment: Data in green, fit in blue, fit with altered parameters in pink and brown.

Note 9 Simulations of collagen gel micromechanics

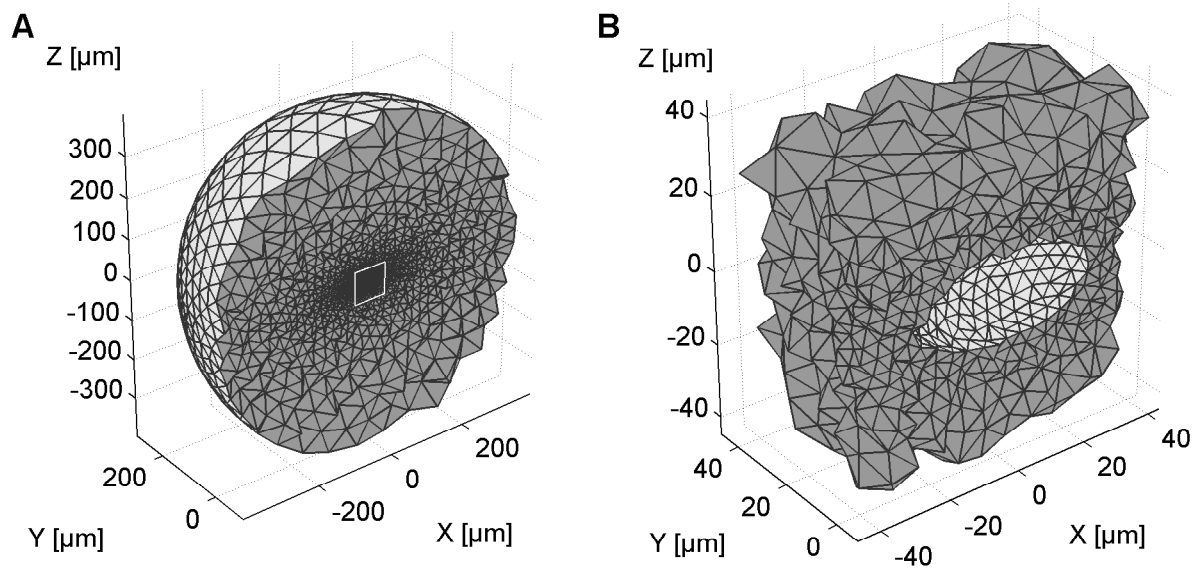


Figure S 6: Cut-open view of a tetrahedral mesh. (A) The whole mesh has a spherical shape (diameter: 800 μm). White box indicates the section shown in B. (B) Magnified view to the ellipsoidal cell inclusion with a length of 50 μm and a width of 30 μm . The mesh consists of 63510 tetrahedra with their density increasing towards the center to achieve a higher resolution at the location of the highest material stresses and deformations.

The Matlab package Distmesh [Persson] is used to generate tetrahedral meshes with full control over geometry as well as node density. The average tetrahedron quality of the used meshes is 0.85. The simulated collagen gel is a sphere with a diameter of at least $800\mu m$ with sticky boundary conditions. In the center of the sphere is an ellipsoidal hole representing the cell. The contractility of the cells is modeled as a Neumann boundary condition (defining the force). We assume that the cell generates a constant stress \mathbf{N}_{cell} throughout its body. From this, the tractions \vec{t} on the cell-gel-interface can be computed by multiplying the normal vector \vec{n} of the boundary tetrahedral faces with the stress tensor

$$\vec{t} = \vec{n} \cdot \mathbf{N}_{cell}$$

For the magnetic tweezer experiments, we simulate the collagen gel response to a force acting on a spherical bead (diameter $5\mu m$). The bead is half embedded in a half space of collagen material so that the bead center is at the level of the collagen surface. The top surface of the collagen gel is modeled as a free boundary condition. The bead is able to rigidly move in the direction of the applied force but is not allowed to rotate.

The boundary value problem (force equilibrium) is solved by minimizing the total strain energy for the given force and displacement constraints. The strain energy density inside each tetrahedron depends only on its deformation gradient \mathbf{F}_T , which in turn depends on the displacements of its nodes. The total strain energy E of the material can be expressed as the sum over the strain energy density $W(\mathbf{F}_T)$ times the volume of every tetrahedron V_T ,

$$E = \sum_T W(\mathbf{F}_T) \cdot V_T$$

We numerically compute the set of second order Taylor-series coefficients \underline{f}_u (Eq. S 16) and $\underline{\underline{K}}_u$ (Eq. S 17) of the total strain energy.

$$E(\underline{u} + \underline{\Delta u}) = E_u + \underline{f}_u \cdot \underline{\Delta u} + \frac{1}{2} \underline{\Delta u} \cdot \underline{\underline{K}}_u \cdot \underline{\Delta u} \quad (21)$$

Here, the dot product in $\underline{f}_u \cdot \underline{\Delta u}$ stands for $\sum_{oj} (\underline{f}_u)_{oj} (\underline{\Delta u})_{oj}$ with $o \in \{\text{free nodes}\}$ and $j \in \{x, y, z\}$. The equilibrium condition $dE/d\underline{u} = -\underline{f}_{ext}$ (Eq. S 14) then reduces to a set of linear equations:

$$-\underline{f}_{ext} = \underline{f}_u + \underline{\underline{K}}_u \cdot \underline{\Delta u} \quad (22)$$

We use the conjugate gradient method to solve this equation. Because the material model is highly nonlinear, we iterate until convergence is reached. The combination of a semi-affine elastic network description with finite element analysis as described here is not limited to collagen gels but may also be used for other biopolymer networks.

We compare simulations of a collagen gel also to simulations of a linear material, for which we chose $w''(\lambda)$ (Eq. 1, main text) to have a constant value such that both material models (linear and non-linear) show the same linear shear modulus of $43 Pa$. The resulting stiffness for the linear material is $\kappa_0/2$ due to the absence of buckling. The linear material shows a constant and symmetric Poisson's ratio of $\nu = 0.25$, whereas the non-linear material shows a asymmetric and strain-dependent Poisson's ratio that can exceed values of $\nu = 4$.

Note 9.1 Isotropic contraction and dilation of a spherical inclusion

To compute the mechanical response of collagen gels to cellular forces, we consider dilating and contractile forces for spherical and elongated cells. First, we analyze the stress and strain distribution in the collagen network around a spherical hole. Dilating forces resemble the situation of a cell that attempts to push through a restricting network

pore, or the situation of a growing cell cluster spheroid inside a collagen matrix. Contracting forces resemble the situation of a cell that spreads in a collagen matrix by adhesive and contractile forces. From the computed stress and strain distribution in the collagen network, we calculate the isotropic pressure inside the hole that is needed to invoke a certain change in hole diameter. In addition to modeling the non-linear behavior of collagen, we perform the same calculation also for a linear elastic material with the same linear shear modulus as collagen but without buckling or strain stiffening. As expected for a linear material, we find for both, contracting and dilating forces the same slope of the pressure versus hole diameter relationship. By contrast, for a non-linear collagen network, a much higher pressure is needed to dilate the hole by more than 10% compared to contracting the hole by 10% (Fig. S 7 C). This asymmetric behavior is attributable to the buckling vs. strain stiffening asymmetry of the fibers. Moreover, we find that during dilation, circumferential fibers close to the hole tauten and bear most of the stress (Fig. S 7 B), forming a stiff ring around the hole like a strait-jacket. This ring effectively shields the bulk of the collagen gel from mechanical stress and prevents the deformations to spread out. The stiffening of circumferential fibers also explains the strong steric hindrance for cell migration in collagen networks with small pore sizes [Friedl 2011, Wolf 2003, Wolf 2013, Zaman 2006]. By contrast, during contraction, the stresses and strains are conducted outwards by the radially stretched fibers and thereby spread over a large distance (Fig. S 7 A), resulting in a much softer response that is nearly indistinguishable from a linear material (Fig. S 7 C). As a possible consequence, the cell may not be able to spread and elongate, similar to the behavior that cells show on very soft 2-D substrates [Engler 2004]. This may explain why many cancer cell lines that are able to metastasize in vivo do not readily migrate in collagen gels [Mierke 2008].

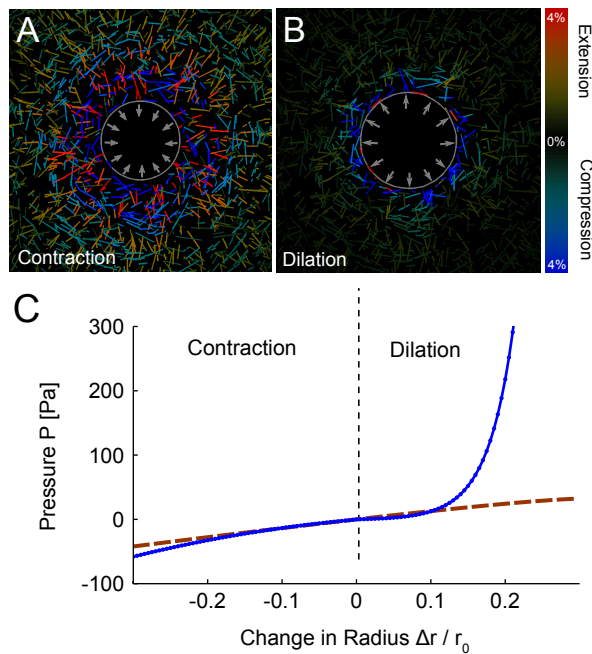


Figure S 7: Collagen gels respond differently to dilating and contracting forces, depending on cell shape. **(A,B)** Fiber deformations around a contracting or dilating three-dimensional ellipsoidal hole. Calculations are performed on a FE grid. For better visualization, only a small number of randomly selected fibers are shown. Blue hues indicate compressed fibers, red hues indicate stretched fibers. Undeformed fibers are not visible. **(A)** During contraction, the strain is effectively conducted outwards and spreads over a large distance. **(B)** Under dilation, the strain is not conducted outwards due to fiber buckling. In addition, circumferential fibers tauten and stiffen. **(C)** The pressure needed to dilate or contract a spherical hole in a linear material (brown) and in a collagen gel (blue), both with the same linear shear modulus. The linear material shows a nearly symmetric response during contraction and dilation. By contrast, collagen gels show a pronounced asymmetric behavior. Strain stiffening is much stronger for dilating than for contracting forces.

Note 9.2 Polarized contraction of an ellipsoid inclusion

To explore how the stiffening response under contraction depends on cell shape, we consider a polarized contracting cell with an ellipsoidal shape, which resembles the common appearance of a migrating mesenchymal cell inside collagen. The cell generates a uniaxially contracting stress (or prestress) throughout its body, resulting in tractions on the cell-gel-interface. We then calculate the elastic response of the collagen to these tractions and the resulting relative cell length changes (cellular contraction). We find that cells with higher aspect ratio exhibit much smaller relative length changes for the same level of prestress (Fig. S 8 A). This equates to a considerably higher apparent stiffness of the material for the more polarized cells. The reason for the apparent stiffening of the material is that the material deformation at the cell poles, for a given cellular contraction, is larger in the case of an elongated cell [Zemel 2010]. Therefore, by shape polarization, the cells can effectively compensate for the small stiffness and weak stiffening response of collagen networks under contraction. Furthermore, in agreement with the literature, we find that matrix displacements around elongated cells in a non-linear collagen gel spread out over much larger distances, up to several hundred microns, compared to displacements in a linear material where they decay much more quickly (Fig. S 8 D) [Abhilash 2014].

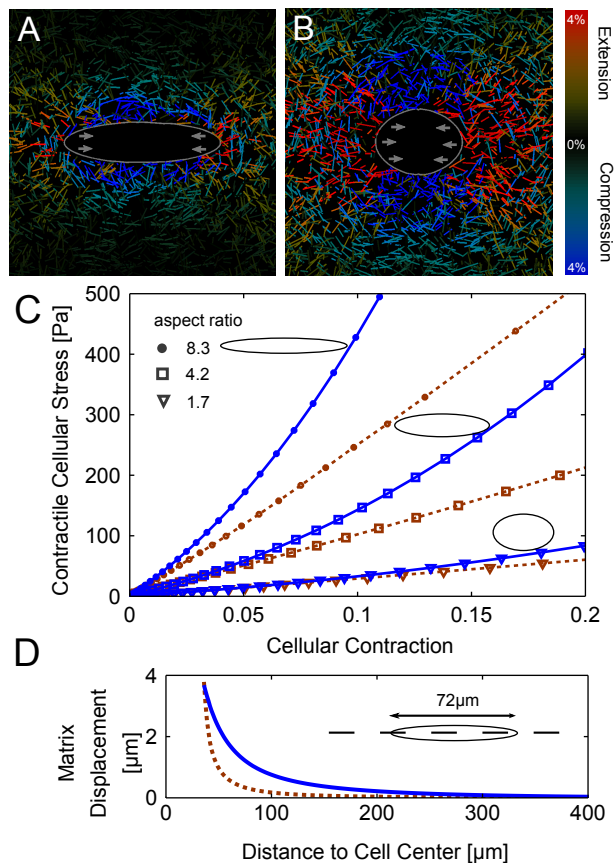


Figure S 8: (A,B) Fiber deformations around a contracting or dilating three-dimensional ellipsoidal hole. Blue hues indicate compressed fibers, red hues indicate stretched fibers. Calculations are performed on a FE grid. For better visualization, only a small number of randomly selected fibers are shown. Undeformed fibers are not visible. Cells in A and B produce the same contractile stress of 51 Pa along their axis of polarization. For a more elongated cell (A, aspect ratio = 4.2), the material responds with less deformation than for a more spherical cell (B, aspect ratio = 1.7). (C) Contractile stress vs. contractile strain for different cell shapes in a linear material (brown) and in a collagen gel (blue) for different cell aspect ratios. (D) Calculated matrix displacement along the primary axis of an elongated cell (aspect ratio = 8.3) for a linear material (brown) and a collagen gel (blue) with the same linear shear modulus. Displacements in the collagen gel decay more slowly.

Note 9.3 Comparison of calculated and measured displacement fields around cells

We compare the calculated matrix displacement fields to measured matrix displacement fields around single cells in a collagen gel [Koch 2012]. We fit the position, orientation and contractile stress of an ellipsoidal inclusion so that the calculated matrix displacements best match the measured displacements around a highly invasive, elongated MDA-MB-231 breast carcinoma cell (Fig. S 9 E), and around a non-invasive, round but highly contractile A-431 vulva carcinoma cell (Fig. S 9 B). The aspect ratios of the contractile ellipsoids are chosen to match the measured cell contours. The measured displacement field around both cells are well reproduced with our constitutive equation (Fig. S 9 A,D), whereas the linear material model fails to reproduce the long-ranging deformations seen in the measurements (Fig. S 9 C,F). For the invasive, elongated breast carcinoma cell, we find that the measured data are best described by an ellipsoid with a uniaxial stress tensor with a magnitude of 289 Pa in the direction of the long cell axis. For the non-invasive, round vulva carcinoma cell, we find the best match with an isotropic stress

tensor with a magnitude of only $12.7 Pa$ in every direction.

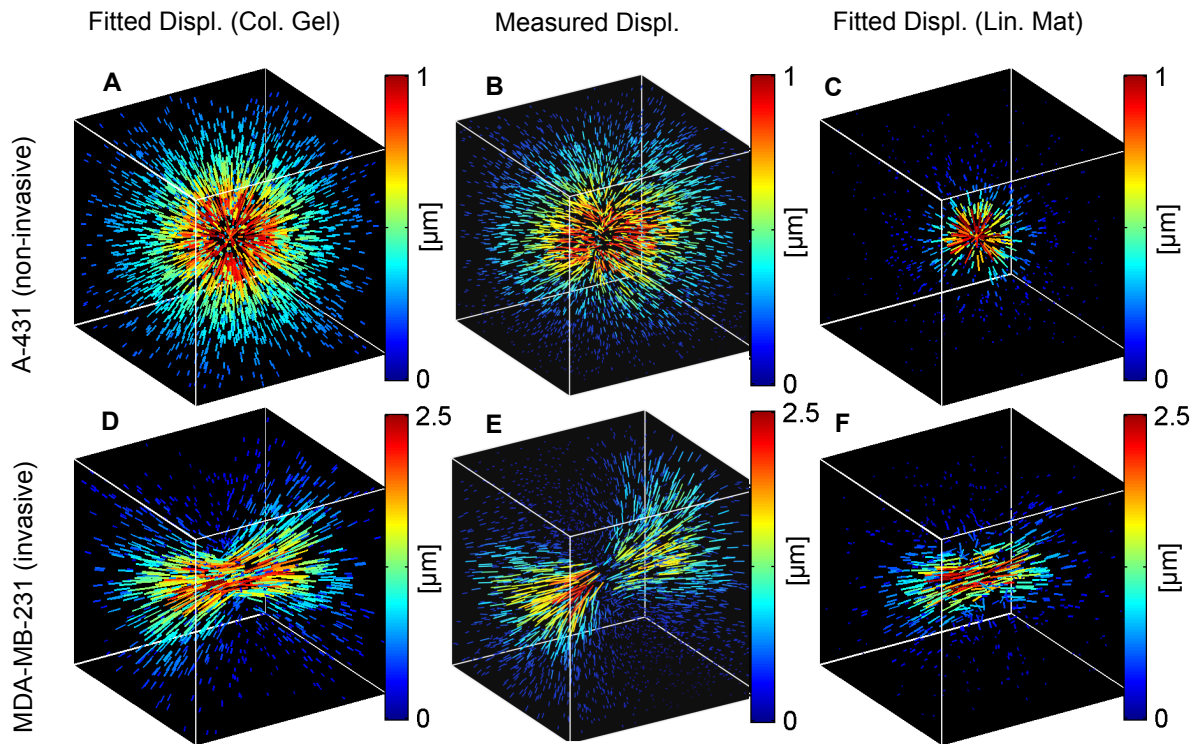


Figure S 9: Measured and calculated displacements in a collagen matrix around non-invasive A-431 vulva cancer cell (upper row), and invasive MDA-MB-231 breast cancer cell (lower row). Colors and line density indicate the magnitude of the matrix displacements. Box size is $200\mu m$. (B,E) Measured matrix displacements from published data [Koch 2012]. (A,D) Calculated displacements for a non-linear collagen gel around an ellipsoidal cell with dimensions taken from measurements [Koch 2012]. The contractile stress ($12.7 Pa$ for A-431 cell, $289 Pa$ for MDA-MB-231 cell) was fitted to match the measured displacements. (C,F) Calculated displacements for a linear material fail to recapitulate the measurements.

Note 9.4 Mechanical anisotropy due to gel geometry

Collagen gels used for cell culture usually have a free top surface. To investigate the effects of this free surface on the local mechanical properties that cells feel at a certain depth in the gel, we compute the apparent stiffness of the gel as a function of depth, for a round cell (Fig. S 10 A: diameter $20\mu m$) as well as an ellipsoidal cell (dimensions $50 \times 15 \times 15\mu m$). The simulated cell culture dish has a width of $800\mu m$. The long axis of the cell is aligned with the direction of the contractile forces. From the simulations, we extract an apparent gel stiffness, which is defined as the amount of contractile stress that the cell generates, divided by the resulting relative contraction of its body. We find that below $200\mu m$, the free surface has no effect on the apparent stiffness. At a depth of $100\mu m$ below the gel surface, however, we see that the anisotropy is highly dependent on the shape of the cell and its orientation relative to the gel surface. We find that the fixed rigid bottom of the dish has no effect on the cell-encountered stiffness (Fig. S 10). In the case of a linear material instead of a collagen gel, we find that the apparent stiffness is independent of the depth and the orientation of the the cell.

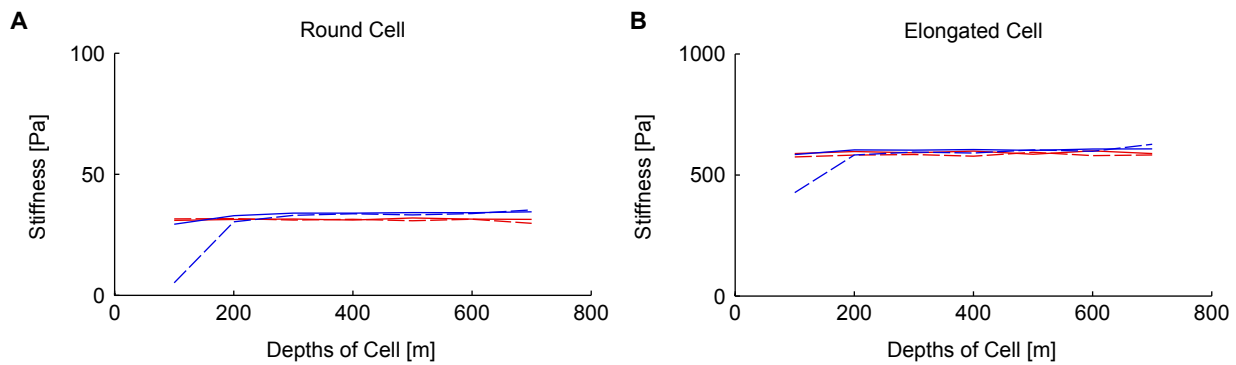


Figure S 10: Apparent stiffness anisotropy resulting from a free surface of a collagen gel for a round cell (A: diameter $20\mu\text{m}$) as well as an ellipsoidal cell (B: dimensions $50 \times 15 \times 15\mu\text{m}$). Red lines show the response of a linear material, blue lines the response of a collagen gel. Dashed lines indicate that the cell is contracting horizontally, whereas solid lines indicates that the cell is contracting vertically. Below a depth of $200\mu\text{m}$ in the gel, the free surface has no effect. The distance to the fixed surface has no effect on the apparent matrix stiffness for distances larger than $100\mu\text{m}$ (depth less than $700\mu\text{m}$).

Note 10 Matrix creep response around a point-like force

To quantify the visco-elastic creep response of the collagen matrix, the displacement of 10 marker beads located near the magnetic bead are measured during application of a constant point-like force (data from Fig. 3 a, see main text). The displacements are normalized by their individual final displacement after 300 s. We find that after 3 s, the matrix displacements have reached 97% of the final displacements, indicating predominantly elastic material properties. As we measure the matrix deformations around cells 30 min after force relaxation, visco-elastic creep can be neglected.

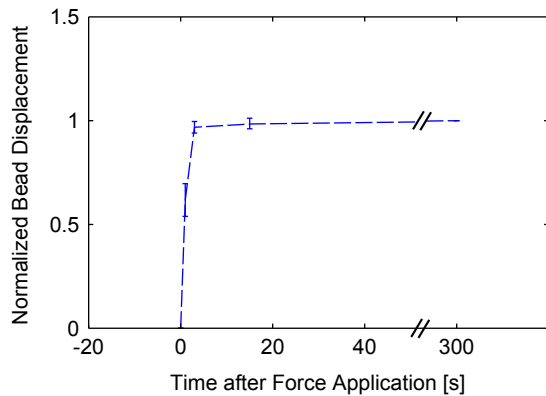


Figure S 11: Displacement of marker beads around a point-like force as a function of the duration of force application. The displacements of the 10 individual beads are normalized by the maximum displacement at 300 s after force application.

Note 11 Test of unconstrained force reconstruction with known point-like force

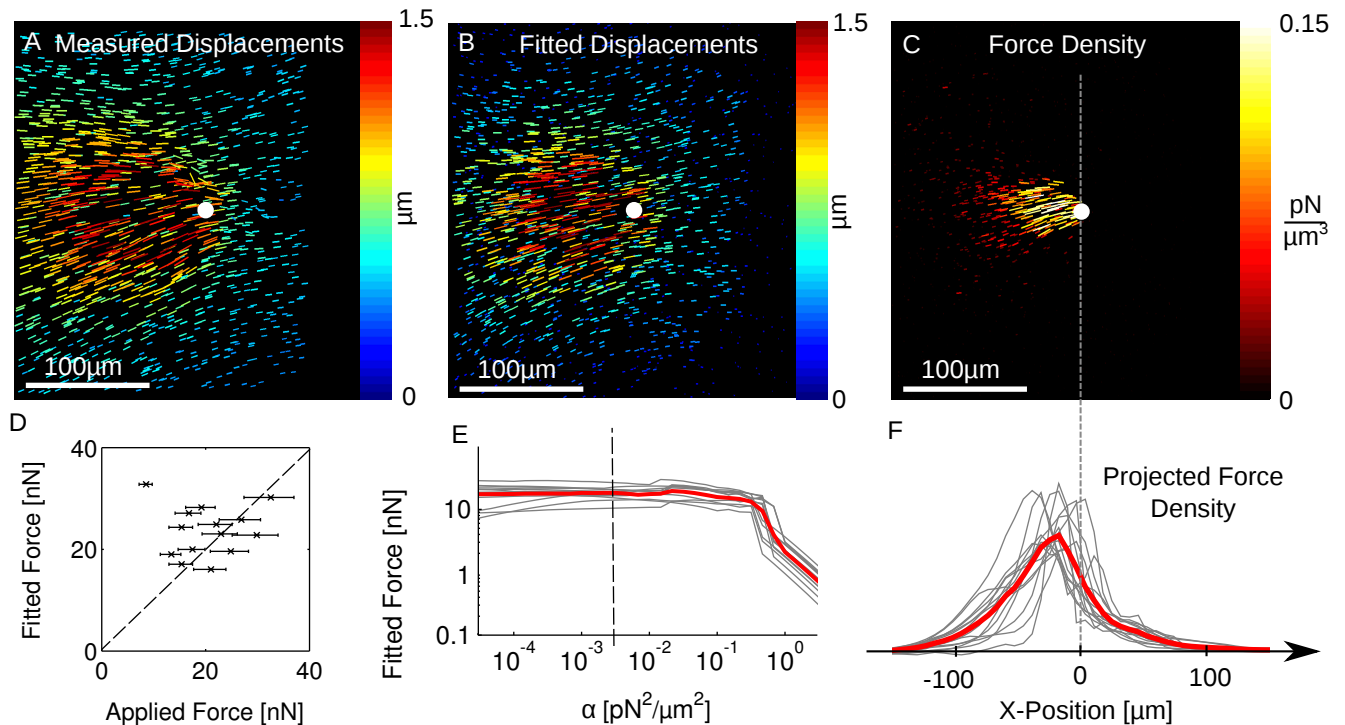


Figure S 12: Experimental validation of the unconstrained force reconstruction method. (A) Measured displacement around a single point-like force on the surface of a collagen gel. (B) Regularized displacements for the same measurement. (C) Force density calculated from the regularized displacements shown in (B). (D) Reconstructed vs. applied force. Horizontal error bars indicate the error in the applied force due to variations in bead size. (E) The reconstructed force amplitude depends only weakly on the choice of the regularization parameter α for values above $\sim 0.3 \text{ pN}^2/\mu\text{m}^2$. Individual measurements in gray, average from 13 measurements in red. Dashed line indicates the value of $\alpha = 0.003 \text{ pN}^2/\mu\text{m}^2$ chosen for all subsequent calculations. (F) Reconstructed force density for each bead is projected onto the x-axis (gray lines). The average force density is shown in red. Zero corresponds to the position of the magnetic bead before force application. Reconstructed forces from a point-like source are systematically shifted to the left ($31 \mu\text{m}$ against the direction of force application) and are spread out with a standard deviation of $29 \mu\text{m}$.

To test our method of unconstrained force reconstruction and to find the appropriate value for the regularization parameter α , we apply a force of 20 nN to a magnetic bead and reconstruct the force from the matrix displacements measured around the bead. This time, we do not constrain the spatial distribution of the force to a point. We find that the algorithm reconstructs a force distribution with a Gaussian shape of $29 \mu\text{m}$ width (Fig. S 12 C) and a center of mass that is scattered with a standard deviation of $5 \mu\text{m}$ between individual measurements. However, the force center is systematically shifted by $31 \mu\text{m}$ in the opposite direction of the applied force (to the left in Fig. S 12 D). This blurring and shifting of the reconstructed force results from the finite size of the elements, measurement noise, numerical regularization, and material inhomogeneities that are not captured by the continuous material model. Nonetheless, the method correctly reconstructs the force magnitude with an error of less than 1% on average and a standard deviation of 30% between individual measurements (Fig. S 12 F). Because the optimal value for the regularization parameter α is unknown, we repeat this computation for multiple values of α . We

find that the total force (vector sum of all forces around the bead) depends only little on α for values below $0.3 \text{ pN}^2/\mu\text{m}^2$. Above this value, the force penalty becomes too high and the total force decays (Fig. S 12 E). Below a value of $0.0003 \text{ pN}^2/\mu\text{m}^2$, noise forces in the bulk of the gel volume begin to appear (Fig. S 16). We choose a value of $0.003 \text{ pN}^2/\mu\text{m}^2$ for all subsequent measurements.

Note 12 Measurement of displacements from confocal reflection stacks

The z-drive of confocal microscopes has a uncertainty in the z-position due to mechanical effects and thermal drift. Alignment of the two image stacks (recorded before (*stack1*) and after (*stack2*) cell force relaxation) is used to remove the z-dependent drift and to reduce the impact of z-drive imprecision. The alignment algorithm is based on a rigid registration method. It replaces every image of *stack2* by a weighted average of images in *stack2* that correlate best with the corresponding image of *stack1*. First, the cross-correlation between a given image *im* of *stack2* with the corresponding image of *stack1* is computed. Next, *im* is shifted by voxel-increments until its cross-correlation with *stack1* reaches a maximum. Every voxel of *im* is then replaced by the average of the *stack2* voxel with the highest cross-correlation and its 26 neighboring voxels, weighted by their respective cross-correlation coefficient. This procedure is repeated for all images of *stack2*. Apart from effectively removing stage drift and z-drive imprecision, this procedure results in a slight low-pass filtering of the images (Fig. S 13) that stabilizes the subsequent step of particle image velocimetry for computing the gel displacement field.

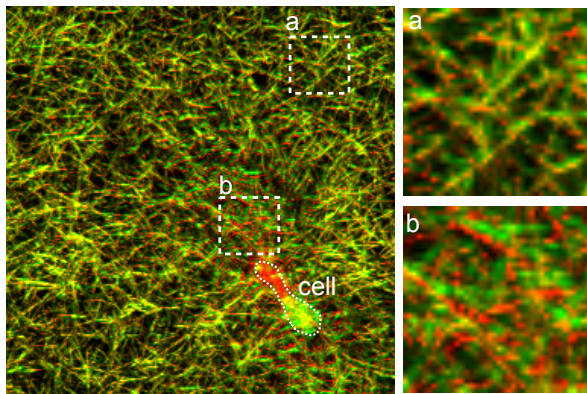


Figure S 13: (Left) Overlay of confocal reflection images of collagen fibers before (red) and after (green) the cell forces were relaxed using cytochalasin D. (Right) Enlarged section of two regions with small (a) and large (b) deformations due to cell forces. In region b, the stressed collagen fibers (red) are displaced towards the cell by approximately $1.5 \mu\text{m}$ relative to the relaxed fibers (green) .

In order to quantify the accuracy of the displacements measured from confocal reflection stacks, we twice recorded a section of a collagen gel without cells. The true displacement field between both stacks is zero at every point. Therefore, non-zero displacements characterize the error of the method. For a section size of 12^3 voxels, each voxel with dimensions $0.72 \mu\text{m}^3$, we find errors of $\sigma \sim 0.06 \mu\text{m}$ in the x, y and z-direction (Fig S 14 A-C). This error depends only weakly on the distance of the confocal z-sections between $0.35 \mu\text{m}$ and $1.4 \mu\text{m}$ (x-y voxel dimensions of $0.72 \mu\text{m}$) (Fig. S 14 D). The error is approximately constant for section sizes between 5^3 and 32^3 voxels (Fig. S 14 E).

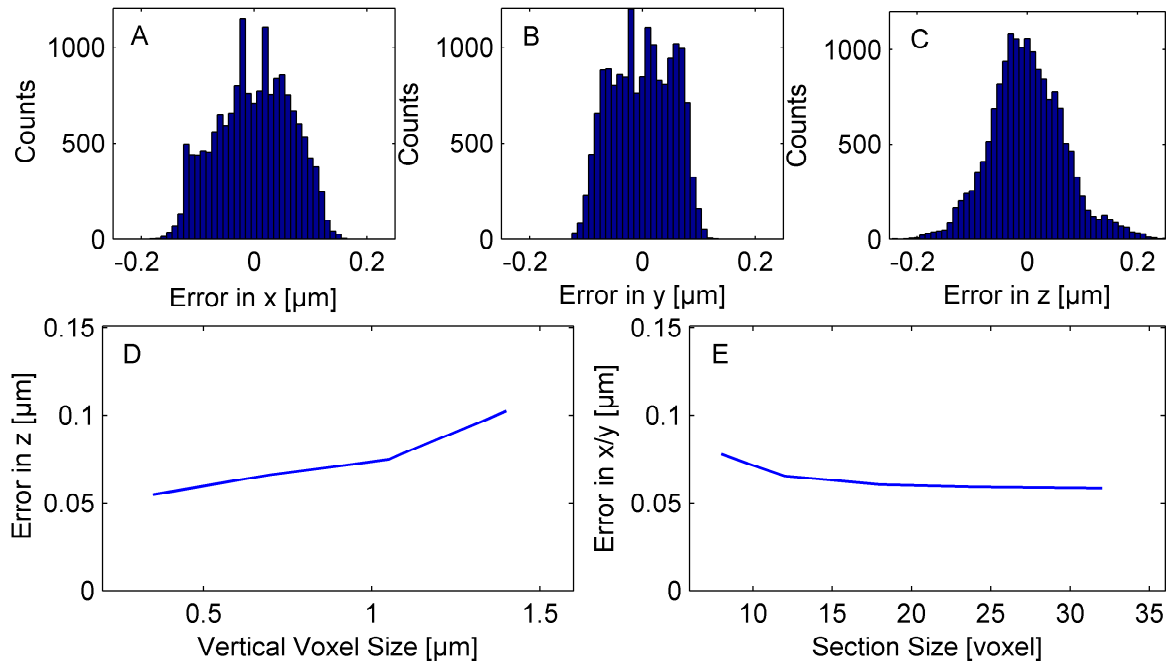


Figure S 14: Error of displacement measurements. (A-C) Error distribution in x (A), y (B) and z (C) direction, measured from two collagen stacks that were recorded consecutively with no cells present. The accuracy of the measured displacements is nearly isotropic. (D) Error in z-direction vs. distance of the confocal z-sections (slice thickness). (E) Error in x/y-direction vs. section size.

Note 13 Analysis of cellular forces

From the unconstrained force reconstruction algorithm, the cellular force field is retrieved as a set nodal forces. As a first step to quantify the cellular forces, the epicenter of the force field \vec{a} is computed. A unique characteristic of the force epicenter is that most forces are pointing directly towards it. Therefore, the epicenter is the point where the norm of the cross-products of the nodal forces with the vectors from their respective nodes to that point is a minimum:

$$Q = \sum_n \left| \vec{f}_n \times (\vec{r}_n - \vec{a}) \right|^2 \quad (23)$$

$n \in \{\text{nodes}\}$

To compute the \vec{a} that minimizes Q , we reexpress Q using the Binet–Cauchy identity [ButlerPC].

$$\begin{aligned} Q &= \sum_n \left| \vec{f}_n \times \vec{r}_n \right|^2 - 2 \cdot (\vec{f}_n \times \vec{r}_n) \cdot (\vec{f}_n \times \vec{a}) + \left| \vec{f}_n \times \vec{a} \right|^2 \\ &= \left| \vec{f}_n \right|^2 \cdot \left| \vec{r}_n \right|^2 - (\vec{f}_n \cdot \vec{r}_n)^2 - 2 \cdot \left(\left| \vec{f}_n \right|^2 \vec{r}_n \cdot \vec{a} - (\vec{f}_n \cdot \vec{r}_n) (\vec{f}_n \cdot \vec{a}) \right) + \left| \vec{f}_n \right|^2 \left| \vec{a} \right|^2 - (\vec{f}_n \cdot \vec{a})^2 \end{aligned}$$

In component notation using the Einstein summation convention, we see that Q is a quadratic function of the epicenter coordinates \vec{a} ,

$$Q = \sum_n f_{ni} f_{ni} r_{nj} r_{nj} - f_{ni} f_{nj} r_{ni} r_{nj} - 2 \cdot (f_{ni} f_{ni} r_{nj} - f_{ni} r_{ni} f_{nj}) \cdot a_j + a_i \cdot (f_{nk} f_{nk} \delta_{ij} - f_{ni} f_{nj}) \cdot a_j$$

$$i, j, k \in \{x, y, z\}$$

where δ_{ij} is the Kronecker delta. Thus we write

$$Q = \text{const} + \sum_n -2 \cdot (f_{ni} f_{ni} r_{nj} - f_{ni} r_{ni} f_{nj}) \cdot a_j + a_i \cdot (f_{nk} f_{nk} \delta_{ij} - f_{ni} f_{nj}) \cdot a_j$$

$$= \text{const} + \sum_n -2B_j a_j + a_i A_{ij} a_j$$

where

$$B_i = \sum_n f_{ni} f_{ni} r_{nj} - f_{ni} r_{ni} f_{nj}$$

and

$$A_{ij} = \sum_n f_{nk} f_{nk} \delta_{ij} - f_{ni} f_{nj}$$

The minimum of Q can be found by setting its derivative with respect to a_i to zero (hence the constant term in Q (independent of a_i) is irrelevant). This gives

$$\frac{\partial Q}{\partial a_i} = 0 = -2B_i + A_{ik} a_k + a_j A_{ji}$$

As the matrix \mathbf{A} is symmetric, it follows that $\mathbf{A} \cdot \vec{a} = \vec{B}$, and the coordinates of the force epicenter are therefore

$$\vec{a} = \mathbf{A}^{-1} \cdot \vec{B}$$

We define the contractility of a cell as the sum of the forces that point towards the epicenter:

$$C_{tot} = \sum_n \frac{\langle \vec{f}_n \cdot (\vec{r}_n - \vec{a}) \rangle}{|\vec{r}_n - \vec{a}|}$$

To quantify the geometry of the cellular force field, we separate the contractile forces of every node into the force contributions from three principal components of an orthogonal coordinate system $\{e_{max}^{\vec{r}}, e_{mid}^{\vec{r}}, e_{min}^{\vec{r}}\}$ that is aligned with the force field of the cell. The contractility can thus be separated into three components $C_{tot} = C_{max} + C_{mid} + C_{min}$. $e_{max}^{\vec{r}}$ is oriented such that the corresponding contractility C_{max} is highest. $e_{max}^{\vec{r}}$ is found by testing a set of 7000 isotropically distributed unit vectors. In the same way, $e_{min}^{\vec{r}}$ is found as the axis of least contractility. $e_{mid}^{\vec{r}}$ is computed as $e_{mid}^{\vec{r}} = e_{max}^{\vec{r}} \times e_{min}^{\vec{r}}$. The polarity P of the force field is given by

$$P = C_{max} / C_{tot} \quad (24)$$

The polarity therefore quantifies the fraction of the contractile force that is oriented in a single direction.

In order to calculate to what extent the cell is affected by the strain stiffening of the collagen matrix, we consider how much work the cell has to invest to deform the collagen by an infinitesimal extra amount ϵ . Because ϵ is

small, we use the Taylor series expansion of the total energy (Eq. S 21).

$$E(\vec{u} + \epsilon \cdot \vec{u}) = E_u + \epsilon \cdot \underline{f_u} \cdot \underline{u} + \frac{\epsilon^2}{2} \cdot \underline{u} \cdot \underline{K_u} \cdot \underline{u}$$

The apparent stiffness of the collagen gel “seen” by the cell is given by the second derivative of the total energy by ϵ .

$$k_{cell} = \frac{\partial^2 E(\vec{u} + \epsilon \cdot \vec{u})}{\partial \epsilon^2} = \underline{u} \cdot \underline{K_u} \cdot \underline{u}$$

We compute k_{cell} for collagen where we either consider the full non-linear stress-strain relationship, or where we consider only the buckling behavior during compression but not the strain-stiffening behavior during extension (material parameter $d_s \rightarrow \infty$). The ratio of both stiffness values quantifies the additional stiffness that the cell encounters because of strain stiffening, and was estimated to be $3.2 \pm 0.5\%$ (mean \pm se) for $n = 38$ MDA-MB-231 breast carcinoma cells (see main text).

The principal stretch, principal stress and principal stiffness of the collagen matrix (see Fig. 5, main text) are calculated from the reconstructed deformation fields as follows. For every tetrahedron T , the direction of the highest positive stretch (\vec{q}) is determined. The associated stress can then be calculated from the stress tensor inside the tetrahedron (Eq. 3, main text) as

$$p_{prin,T} = \sum_{i,j} N_{Tij} q_i q_j$$

The principal stiffness is computed as the derivative of the principal stress with respect to the deformation in the direction of the principal stretch, utilizing the stiffness tensor \mathbf{K} (Eq. S 1)

$$k_{prin,T} = \sum_{i,j,k,l} K_{Tijkl} q_i q_j q_k q_l$$

For an isotropic linear material, the principal stiffness is (Eq. S 2)

$$k_{prin} = \frac{Y \cdot (1 - \nu)}{(1 + \nu)(1 - 2\nu)}$$

Where Y is the Young's modulus and ν is the Poisson's ratio.

Note 14 Test of force reconstruction algorithm with synthetic data

We test the robustness of the unconstrained force reconstruction method using synthetic data, for which measurement noise and signal level (contractility of a cell) are precisely controlled. The calculated deformations around a polarized contracting ellipsoidal cell (dimensions $15 \times 15 \times 50 \mu m$) as discussed in section 6.2 are used as a signal. The contractility of the cell is chosen to be $0 nN$, $5 nN$, $30 nN$ or $100 nN$, respectively. The displacement field is interpolated onto a regular mesh (grid constant = $15 \mu m$). To account for measurement error, Gaussian noise of varying amplitudes ranging from $0 - 500 nm$ is added to the displacements of each node. Fig. S 15 shows the reconstructed total contractility as a function of the regularization parameter α for different true contractilities and different noise levels. The total reconstructed contractility is largely independent of α for α -values above $3 \cdot 10^{-4} \frac{\mu m^2}{pN^2}$ and below $10^{-2} \frac{\mu m^2}{pN^2}$. For higher values of α , the contractility approaches zero as cellular forces are excessively penalized. For intermediate α -values, the reconstruction algorithm slightly underestimates the true contractility of the cell. In addition, higher noise levels lead to a larger underestimation of the true contractility, but even for the highest noise level of $500 nm$, the error remains below $15 nN$. For a noise level of $60 nm$ and

α -value of $3 \cdot 10^{-3} \frac{\mu m^2}{pN^2}$ as in our measurements, the relative error is negligible. The underestimation of large contractilities in the absence of noise (10% for a contractility of 100 nN) arises because the deformation field around the ellipsoidal cell is calculated from the known surface tractions, whereas the reconstruction algorithm assumes a continuous force field. As further validation of the algorithm we repeat this procedure also for different mesh sizes. We find no appreciable differences in the reconstructed contractility. For a true contractility of 30 nN and a noise level of 100 nm, the reconstructed contractility is 31.3 nN for a mesh size of 7.5 μm , 29.1 nN for a mesh size of 10 μm and 29.9 nN for a mesh size of 15 μm .

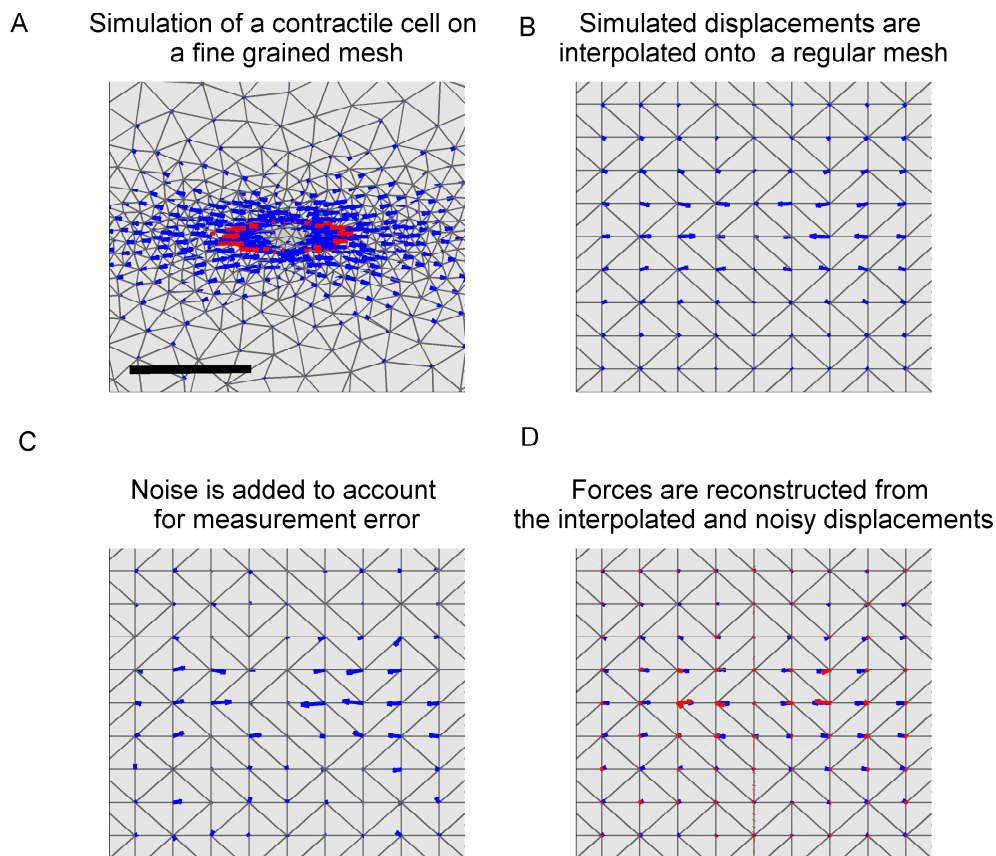


Figure S 15: (A) Cut-open view of the finite element mesh around a contractile cell. The cell is modeled as an ellipsoidal hole inside a continuous material. The cell generates traction forces (red arrows) at its poles with a total contractility of 30 nN. The matrix reacts to these forces through displacements (blue arrows). (B) The matrix displacements in (A) are interpolated onto a regular grid. (C) To account for measurement error, Gaussian noise (300 nm) is added to the displacements. (D) The cellular forces (red arrows) are reconstructed by unconstrained force reconstruction. The reconstructed total contractility is 28.7 nN. Scalebar is 50 μm .

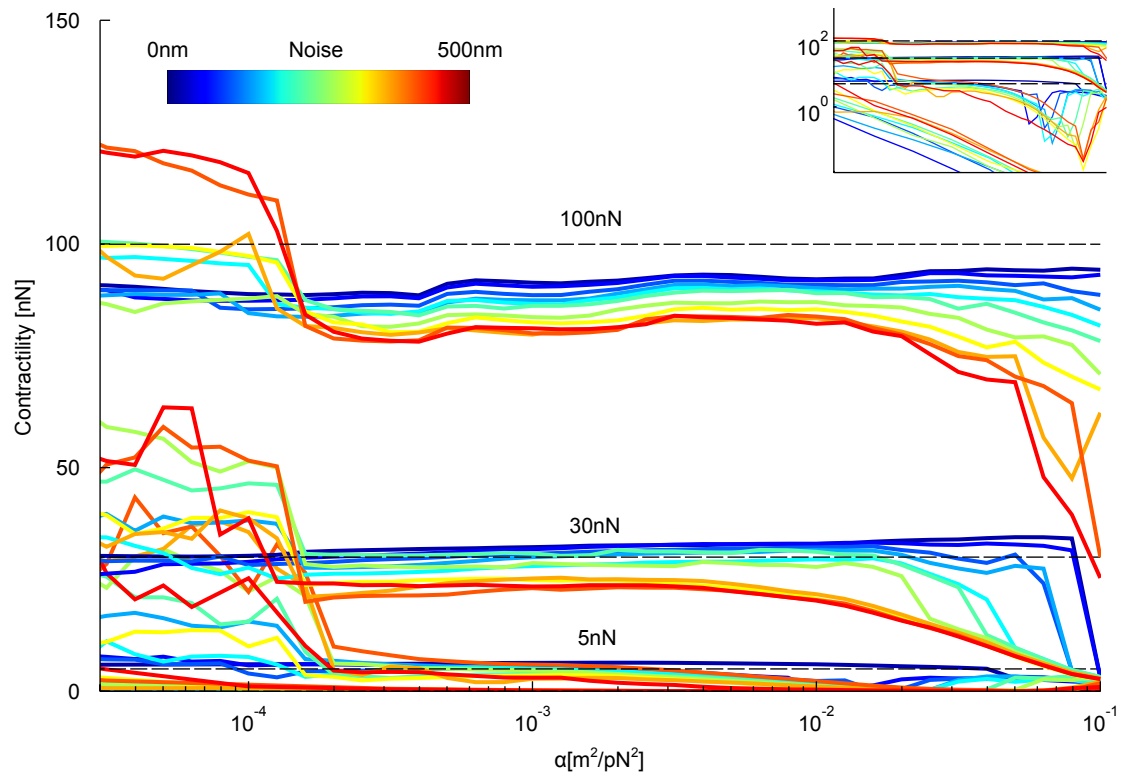


Figure S 16: Influence of the regularization parameter α on total reconstructed contractility for different true contractilities (0 nN, 5 nN, 30 nN and 100 nN) and different noise levels (corresponding to line color).

As described in the main text, we find that the reconstructed forces are systematically shifted away from the point of force application, both for point-like applied forces as well as cellular forces. To test whether this is due to the unconstrained force reconstruction algorithm or due to the inhomogeneity of the material, which is not captured by our material model, we analyze this shift in simulated data. The material model for the simulation is the same as for the reconstruction and does not comprise material inhomogeneity. The contractility of the simulated cell is 30 nN. The simulated displacements are interpolated onto a regular mesh with a mesh size of $7.5 \mu\text{m}$. Then 100 nm Gaussian noise is added to the displacements of each node before the unconstrained force reconstruction algorithm is used to reconstruct the cellular forces from these displacements. We integrate the resulting force density along the axes perpendicular to the cell orientation. In the resulting plot we see that the reconstructed force maxima remain close to the cell surface (Fig S 17). This points towards the neglected material inhomogeneity as the main reason for the systematic shift of the reconstructed forces.

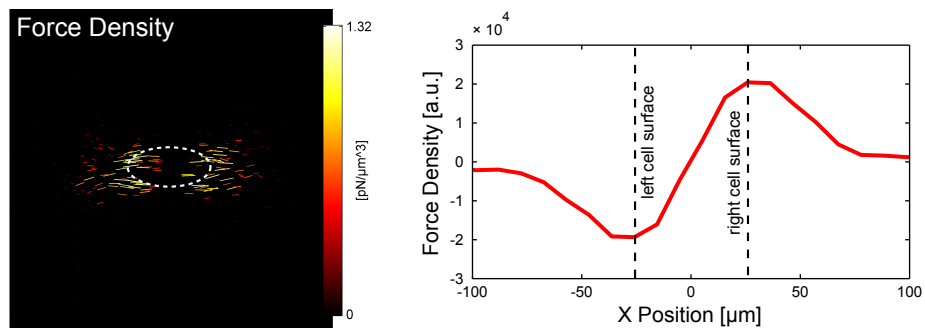


Figure S 17: (left) Force density plot of reconstructed forces (right) Force density (red) reconstructed from simulated data projected along the axis of cell orientation. The force maxima are not notably shifted away from the cell (dashed).

As with all force microscopy methods, the sensitivity depends foremost on the resolution and accuracy of the measured displacement field. Fig S 18 shows the erroneously reconstructed contractility versus the displacement noise level using the concentration-dependent material parameters for collagen gels with concentrations of 0.6, 1.2 and 2.4 mg/ml. For the MDA-MB-231 carcinoma cells investigated in our study (contractility ≈ 40 nN) and the noise in the displacements that we achieve with our confocal microscope (60 nm rms), the relative error is below 5%, and the detection limit for the total cellular contractilities is ~ 2 nN. We also analyze the local error in the reconstructed force density as a function of the measurement noise for different collagen concentrations. We find that the reconstructed error remains below 10^{-5} pN/ μm^3 . This is several orders of magnitude below typical values of $\sim 10^{-1}$ pN/ μm^3 that we measure for cells.

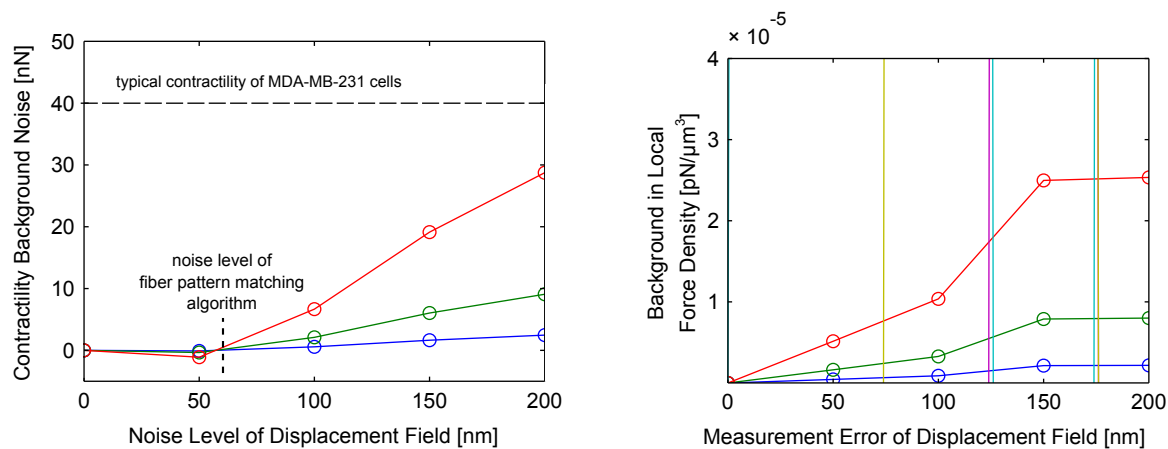


Figure S 18: Contractility background noise (left) and background in local force density (right) for different collagen concentrations (0.6 mg/ml in blue, 1.2 mg/ml in green and 2.4 mg/ml in red) versus noise level of measured displacements, in absence of true cellular forces.

Note 15 Robustness of unconstrained force reconstruction tested on real data

To test the robustness of the unconstrained force reconstruction method on a dataset of a contractile breast carcinoma cell, we delete the measured displacement information on a fraction of the nodes and let the algorithm reconstruct the contractile force. This is implemented by altering the \underline{P} matrix (see method description in the

main text) that flags valid displacement entries. We find that up to 75 % of the displacement information can be deleted without appreciable deviations of the reconstructed total contractility. When more than 75 % of the displacement information is deleted, however, the algorithm can no longer separate signal from noise, and the reconstructed total contractility decays.

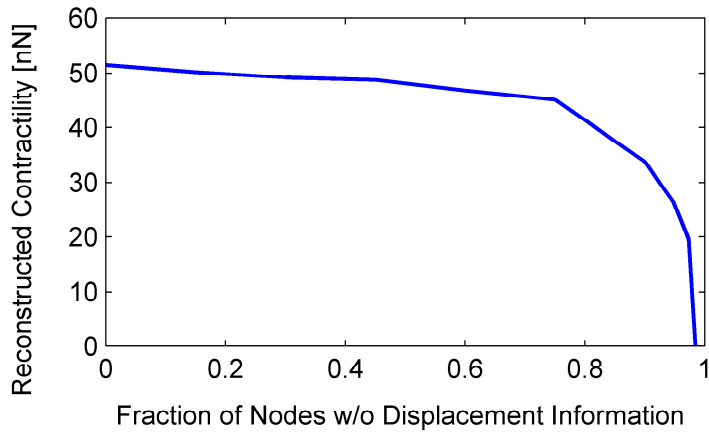


Figure S 19: Total reconstructed contractility vs. fraction of nodes without displacement information.

Note 16 Computation time of unconstrained force reconstruction software depending on mesh density

The computation time of the algorithm depends on the grid constant of the finite element mesh. For values between $5 \mu m$ and $20 \mu m$ we find that the computation time scales linearly with the number of mesh points and therefore with the grid constant to the -3 rd power. For a grid constant of $7.5 \mu m$ as used here, the total computation time is $\sim 3 h$ running on a single Pentium E6500 CPU core. This computation time includes the reconstruction of the displacement field from confocal reflection data. On a more modern Intel core i5-3470 CPU the computation time is only $53 min$ running on a single core at a grid constant of $7.5 \mu m$.

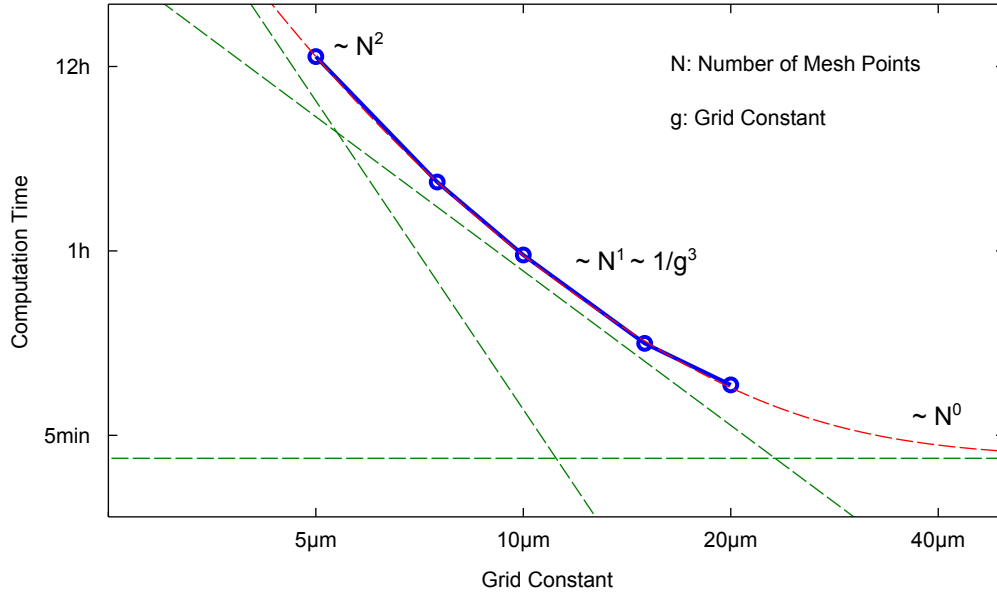


Figure S 20: Total computation time vs. grid constant of the finite element mesh. Data are shown in blue. The fit (red) is a second order polynomial in the number of mesh points (N). The green lines correspond to the 3 terms of the polynomial. In the relevant regime between $5\ \mu\text{m}$ and $20\ \mu\text{m}$, the computation time scales approximately linearly with the number of mesh points.

Note 17 Comparison of constrained and unconstrained reconstruction of cell forces

In the main text, we compare constrained and unconstrained force reconstruction for the same data set of matrix displacements around a point-like force applied to the surface of a collagen gel. There we find that the constrained force reconstruction has a slightly higher accuracy in the localization of forces, whereas the unconstrained force reconstruction has a higher accuracy in the force magnitude. To compare force magnitude and localization accuracy of the unconstrained and constrained force reconstruction algorithm, when measuring cells, we record the matrix displacement field around 15 HT1080 cells stably expressing TagRFP inside a $1.2\ \text{mg/ml}$ collagen gel. From the fluorescence stack, we extract the points of the finite element mesh with a distance to the cell of less than half a mesh size ($3.75\ \mu\text{m}$). For these points, we set the force penalty A_{ii} to 0 and for all other points to $0.003\ \text{pN}^2/\mu\text{m}^2$, instead of letting the algorithm find the values of A_{ii} through the iterative approach described in the main text. Thereby we constrain the cellular forces to the cell surface. We confirm that the reconstructed cell forces only appear on the cell surface (Fig. S 21 E). The displacement field that we fit using the constrained algorithm, however, overestimates the measured matrix displacements or the displacements fitted with the unconstrained method, with maximum values that appear closer to the cell (Fig. S 21). The reconstructed contractilities, however, deviate not as strongly ($69 \pm 15nN$ for the constrained and $63 \pm 13nN$ for the unconstrained case (mean \pm se of $n=15$ cells)) as the differences in the fitted displacement fields would suggest. We find also no significant differences for the reconstructed cell polarity (0.56 ± 0.11 for the constrained and 0.42 ± 0.07 for the unconstrained case (mean \pm se of $n=15$ cells)). We see this as confirmation that the unconstrained force reconstruction is not inferior to a constrained method for computing total contractility or force polarity.

NEW NEW NEW

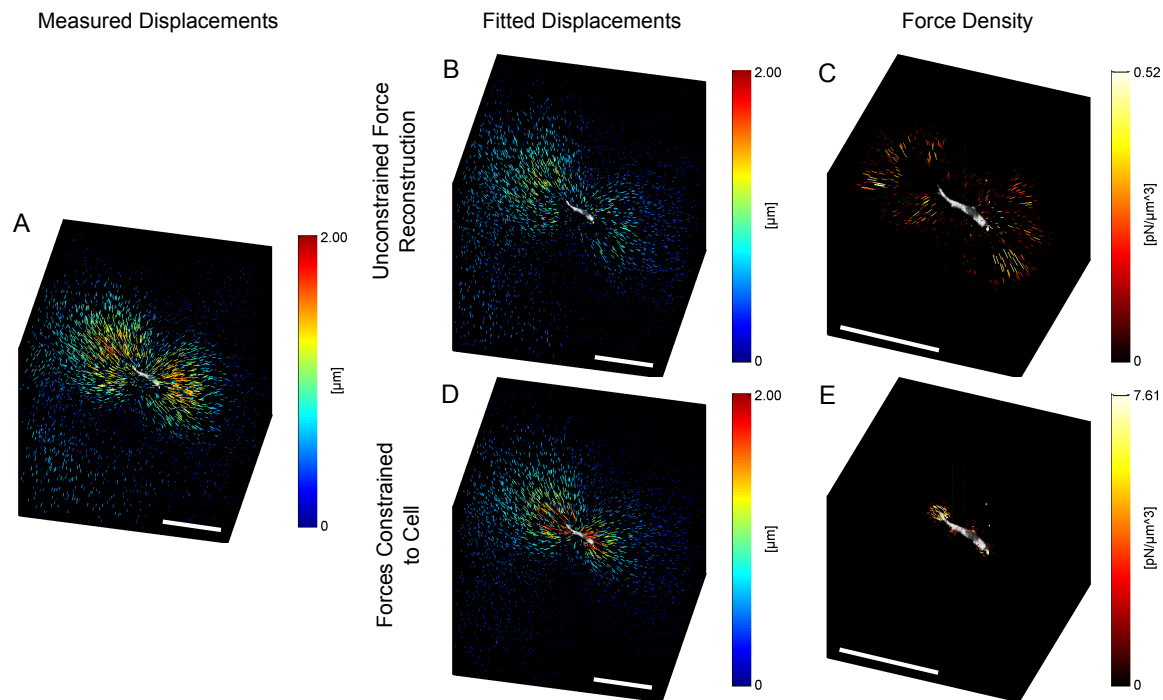


Figure S 21: Constrained and unconstrained reconstruction of cellular forces. (A) Measured displacement field around HT1080 cell stably expressing TagRFP (shown in gray). (B) Displacement field fitted using unconstrained force reconstruction. (C) Force density obtained from unconstrained force reconstruction. (D) Displacement field fitted while constraining the forces to the cell surface. The maximum displacements are higher and appear closer to the cell when compared to (A) and (B). (E) Force density obtained from constrained force reconstruction. Cell forces only appear on the cell surface. The force density therefore has higher maximum values. Scalebar is 100 μm .

Note 18 Influence of mesh size and choice of α -value on unconstrained force reconstruction

For 3 different mesh sizes ($5 \mu\text{m}$, $7.5 \mu\text{m}$ and $10 \mu\text{m}$), we calculate the force density around an MDA-MB-231 cell embedded in a 1.2 mg/ml collagen gel using the unconstrained force reconstruction method with a range of values for the regularization parameter α between $10^{-4} \text{ nN}^2/\mu\text{m}^2$ and $1 \text{ nN}^2/\mu\text{m}^2$. For all mesh sizes, the contractility decreases with higher values of α . For an intermediate range of α -values, however, the contractility is nearly constant. We observe that both, this α -range and the corresponding contractility shift towards higher values with decreasing mesh size (Fig. S 22 A).

To select the appropriate α -value for the chosen mesh size, we analyze the reconstructed force field around the cell for different α -values. If α is chosen too low, noise forces appear everywhere; if α is too high, the cellular forces are smeared out also towards regions far outside of the cell. To quantify this effect, we plot the force density as a function of the distance to the cell surface and compute the first moment, which gives the average distance between the force vectors and the cell surface. For all three mesh sizes, the average force distance to the cell surface shows a minimum (Fig. S 22 B). This minimum corresponds to a reconstructed force field that neither is excessively smeared out nor excessively noisy, and thus represents an optimum. The optimum α shifts towards lower values with increasing mesh size. Fig S 22 C-E shows the reconstructed force field for three different mesh sizes and α -values as indicated by the dashed lines in Fig S 22 A+B.

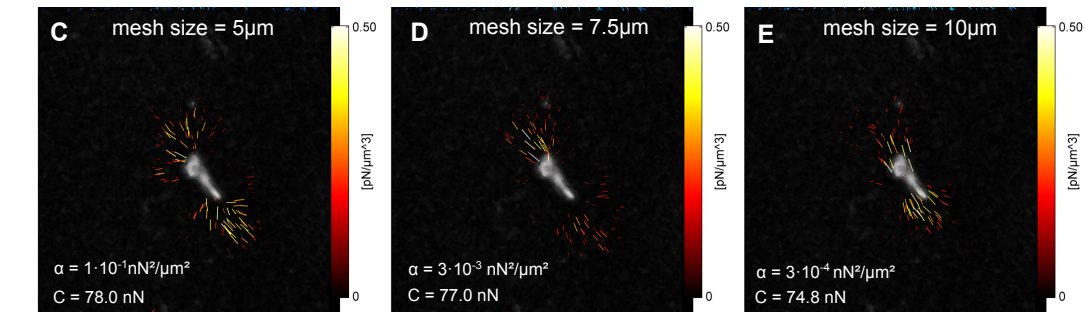
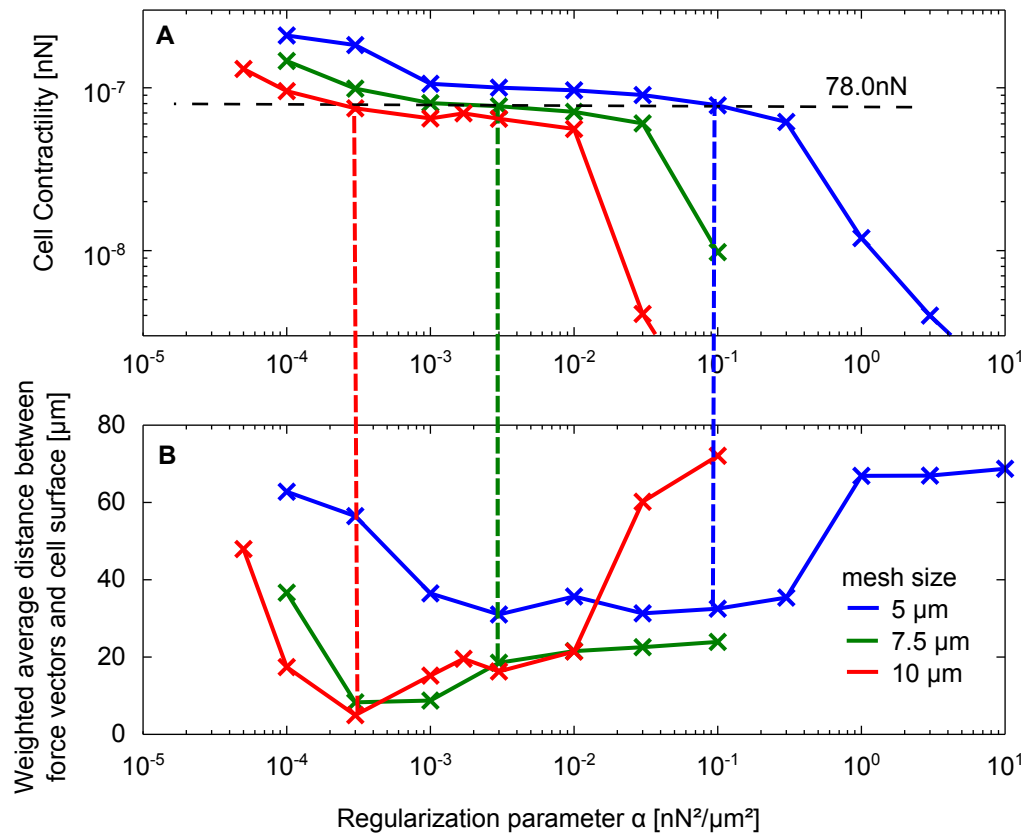


Figure S 22: (A) Cell contractility as a function of the regularization parameter α for three different mesh sizes (5 μ m in blue, 7.5 μ m in green and 10 μ m in red). In all cases, the contractility decreases with higher values of α . For intermediate values of α , the contractility is nearly constant. (B) Weighted average distance of the reconstructed force vectors to the cell surface as a function of the regularization parameter α for the same mesh sizes as shown in (A). In all cases, the distance shows an minimum for intermediate values of α that shifts towards lower α -values for increasing mesh sizes. (C,D,E) Reconstructed force field for three different mesh sizes and α -values as indicated by the dashed lines in (A) and (B).

Note 19 3-D force fields around MDA-MB-231 cells

In the following we present the individual force fields around all measured MDA-MB-231 breast carcinoma cells (n=38) in collagen gels with a collagen concentration of 1.2 mg/ml.

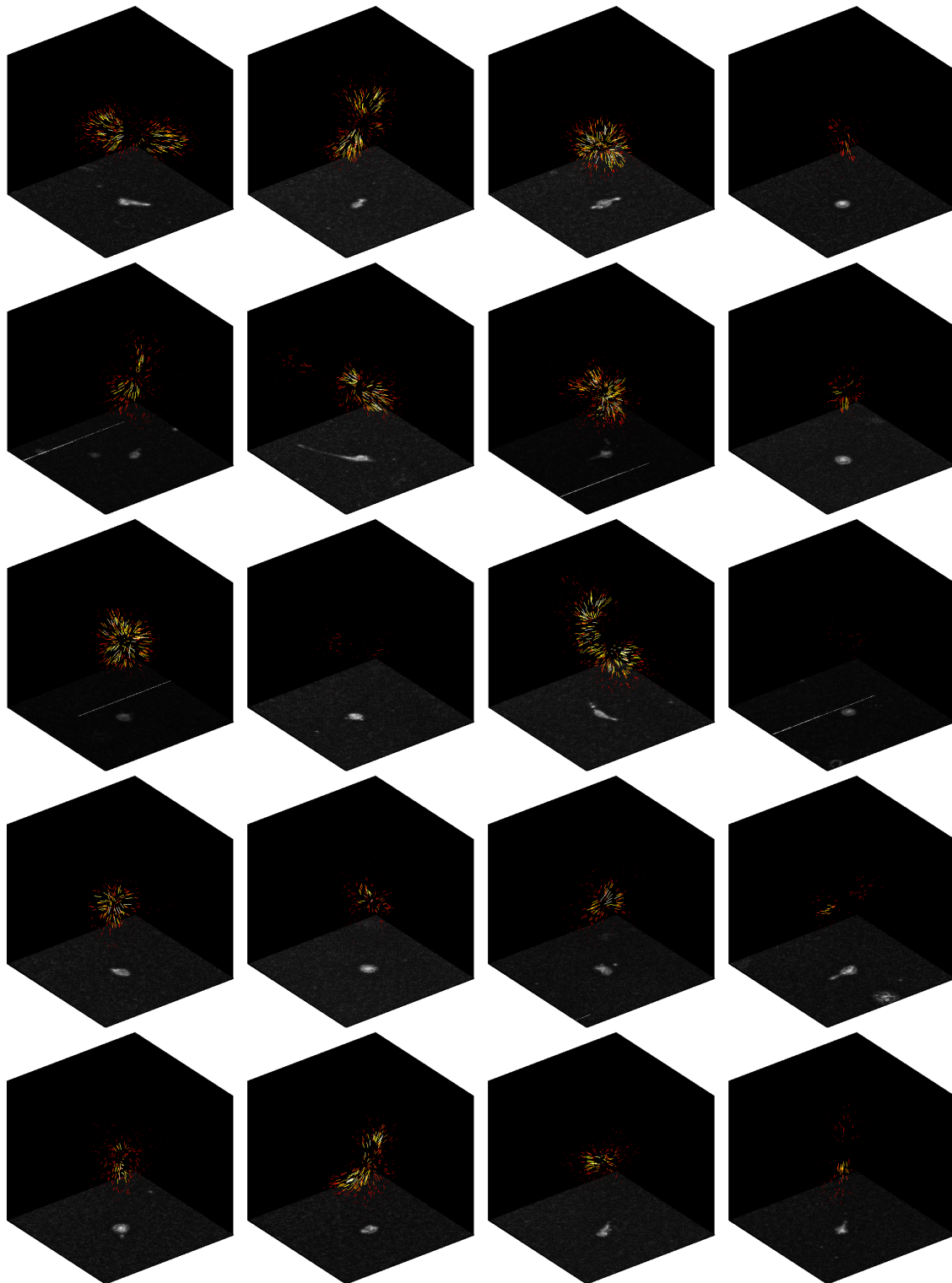


Figure S 23: 3-D force density plots around different MDA-MB-231 breast carcinoma cells. Arrow density and color corresponds to the local force magnitude. For colorbar, see Fig. S 24. Total displayed volume is a cubic box with edge length of $200\ \mu\text{m}$. The bottom face of the displayed box shows a brightfield z-projection of the cell.

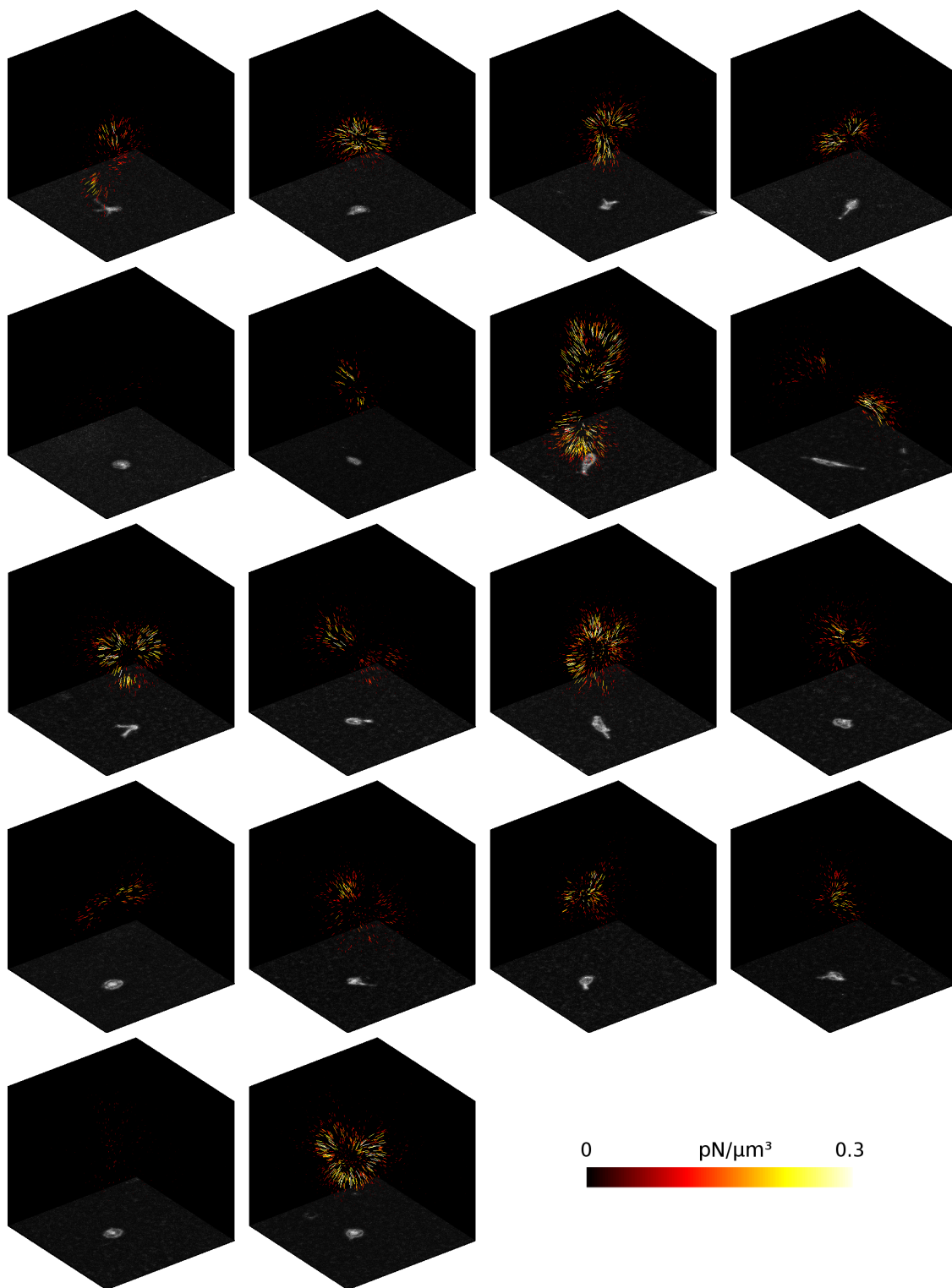


Figure S 24: For caption see Fig. S 23

Note 20 Lagtime dependent cross-correlations of cell shape, motility and contractility

As described in the main text, we simultaneously measure the time course of contractility, cell elongation, migration persistence and migration activity (Fig. 6, main text). The following figure displays the full lag time depend cross-correlation matrix. The correlation functions were computed for every cell separately and then normalized by the variance over all cells and time-points. Therefore, the auto-correlation functions for zero lag can deviate from unity for individual cells, but not on average. The error values were calculated by bootstrapping.

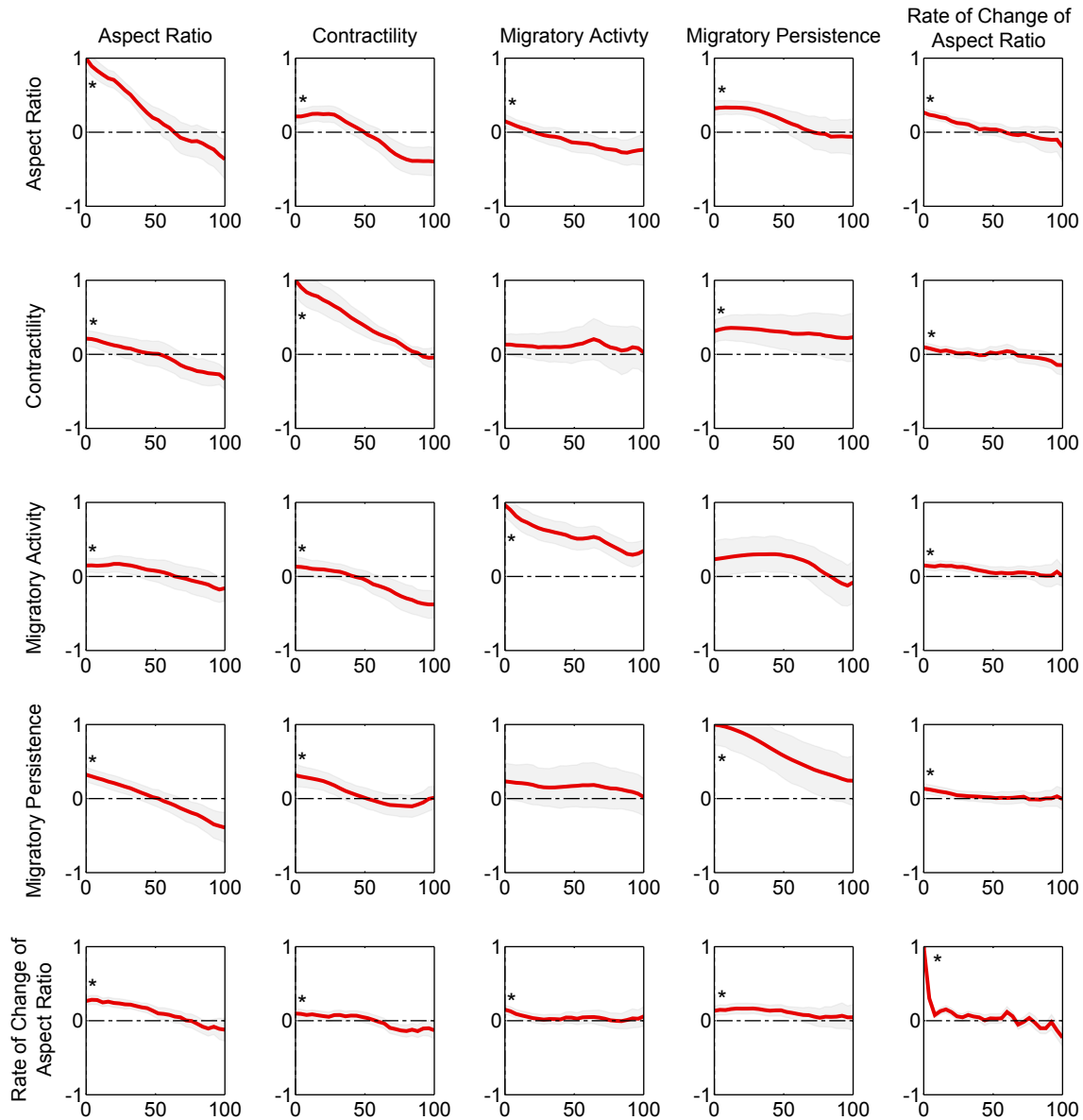


Figure S 25: Lagtime dependent cross-correlation matrix of the aspect ratio, contractility, migratory activity, migratory persistence and protrusive activity. All x-axes display the lagtime in minutes. A star indicates that the correlation is significant ($p < 0.05$) for zero lag.

Note 21 Influence of collagen concentration on cell contractility

In the main text, we describe that the cells are less elongated in the stiffer and denser collagen gels. To test whether impeded cell elongation is the reason why the cells are not able to contract more strongly in stiffer gels, as cells plated on stiffer 2-D gels normally do [Trichet2012], we analyze the sub-population of cells that have an aspect ratio of 2.0 or higher. The aspect ratio of the cells was determined from brightfield projections of the cells. We find that the elongated cells grown in collagen gels with a concentration of 1.2 mg/ml indeed show a significantly increased contractility compared a sub-population of similarly elongated cells grown in collagen gels with a concentration of 0.6 mg/ml . For cells grown in collagen gels with a collagen concentration of 2.4 mg/ml , we are not able to resolve differences do the low number of cells that have a sufficiently elongated shape.

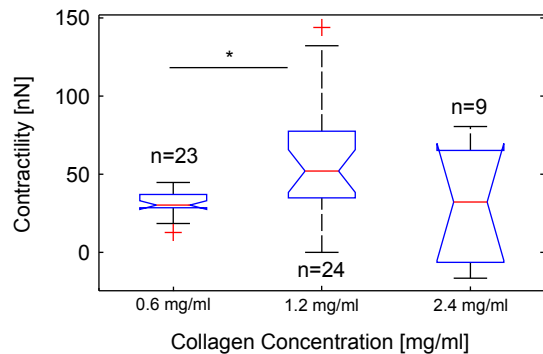


Figure S 26: Cell contractility of elongated cells measured in collagen gels with different collagen concentration. Only cells with an aspect larger than 2.0 were included in this analysis.

References

- [Abhilash 2014] **Remodeling of Fibrous Extracellular Matrices by Contractile Cells: Predictions from Discrete Fiber Network Simulations**, Biophysical Journal, 2014, Abhilash AS, et al.
- [ButlerPC] Personal communication, 2005, Butler JP
- [Brown 2009] **Multiscale mechanics of fibrin polymer: gel stretching with protein unfolding and loss of water**, Science, 2009, Brown AE, et al.
- [Engler 2004] **Substrate compliance versus ligand density in cell on gel responses**, Biophysical journal, 2004, Engler A, et al.
- [Friedl 2011] **Nuclear mechanics during cell migration**, Current opinion in cell biology, 2011, Friedl P, Wolf K, & Lammerding J
- [Koch 2012] **3D Traction Forces in Cancer Cell Invasion**, PLOS one 7, 2012, Koch TM, et al.
- [Legant 2010] **Measurement of mechanical tractions exerted by cells in three-dimensional matrices**, Nature Methods, 2010, Legant WR, et al.
- [Mierke 2008] **Breakdown of the endothelial barrier function in tumor cell transmigration**, Biophysical journal, 2008, Mierke CT, et al.
- [Ogden] **Non-Linear Elastic Deformations**, Dover edition, 1943, by R.W. Ogden

- [Persson] **A Simple Mesh Generator in MATLAB**, SIAM Review, 2004, *P.O. Persson, G. Strang*
- [Trichet2012] **Evidence of a large-scale mechanosensing mechanism for cellular adaptation to substrate stiffness**, PNAS, 2012, L. Trichet, J. Le Digabel, J. Hawkins, S. Vedula, M. Gupta, C. Ribault, P. Hersen, R. Voituriez, B. Ladoux
- [Wolf 2003] **Compensation mechanism in tumor cell migration: mesenchymal-amoeboid transition after blocking of pericellular proteolysis**, Journal of cell biology, 2003, *Wolf K, et al.*
- [Wolf 2013] **Physical limits of cell migration: Control by ECM space and nuclear deformation and tuning by proteolysis and traction force**, Journal of cell biology, 2013, *Wolf K, et al.*
- [Zaman 2006] **Migration of tumor cells in 3D matrices is governed by matrix stiffness along with cell-matrix adhesion and proteolysis**, PNAS, 2006, *Zaman MH, et al.*
- [Zemel 2010] **Optimal matrix rigidity for stress fiber polarization in stem cells**, Nature Physics, 2010, *Zemel A, et al.*
- [ZienkiewiczV1] **The Finite Element Method - Volume 1: The Basis**, 2000, *O.C. Zienkiewicz & R.L. Taylor*